MilliporeSigma

Material Matters™

VOLUME 14 • NUMBER 2

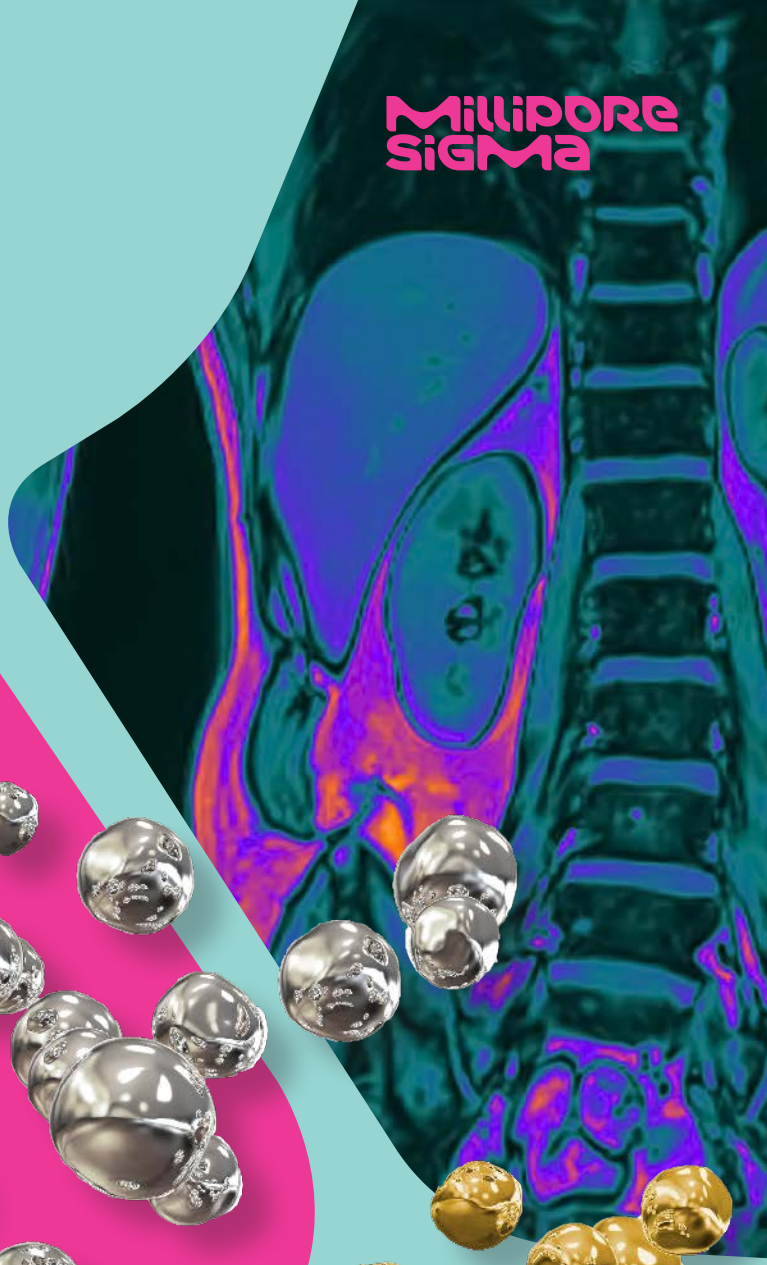

Nanomaterials for Bioassays and Imaging

FLUORESCENT NANOMATERIALS FOR BIOIMAGING: Considerations of Particle Brightness, Photostability, and Size

Applications of QUANTUM DOTS in Bioimaging and Bioassays

Recent Developments in MAGNETIC IRON OXIDE NANOPARTICLES for Non-Invasive Bioimaging

Increasing the Sensitivity of LATERAL FLOW DIAGNOSTIC ASSAYS with Ultra-Bright Gold Nanoparticle Nanoshell Reporters

The life science business of Merck KGaA, Darmstadt, Germany operates as MilliporeSigma in the U.S. and Canada.

Material Matters™
VOL. 14 • NO. 2

Introduction

Taryn L. Fuhrman-Hall, M.B.A.
Product Manager, Materials Science

Welcome to the second issue of *Material Matters*™ for 2019, focused on nanomaterials for bioimaging and diagnostic assays. The conceptual framework for nanomaterials was first proposed in 1959 by Nobel Laureate Prof. Richard Feynman, and in the last 25 years has seen continued, substantial growth in scientific publications describing the synthesis and applications of different nanostructured materials. The unique properties of nanomaterials have made them an engine of innovation for biomedical, electronics and energy research. For biomedical applications, the similarity in the size of nanomaterials to that of proteins and other cellular components (≤100 nm) creates additional interactions with utility in various diagnostic applications.

In the first article, Professor Xiaohu Gao (University of Washington, USA) provides an overview of recent quantum dot (QD) advancements and their potential for advancing bioassay and bioimaging technologies. Three general applications for QDs are reviewed, including sensing and detection, *in vitro* labeling and imaging, and *in vivo* imaging.

Professor Marco Torelli (ARC Centre of Excellence for Nanoscale BioPhotonics & School of Science, Australia) examines fluorescent nanomaterials for use in bioimaging applications in the second article. Fluorescent nanomaterials have many beneficial capabilities allowing them to achieve successful implementation in a variety of applications. This article reviews current state-of-the-art materials, focusing on fluorescence brightness, photostability, and size, and relates them to emerging applications.

As advancements in non-invasive imaging technologies continue to grow, new nanomaterial-based contrast agents are being investigated. In the third article, Professor Hui Mao (Emory University School of Medicine, USA) explores the use of superparamagnetic iron oxide nanoparticles (INOPs) that offer an alternate contrast-enhancing mechanism. This article focuses on shape control and renal-clearable sub-5 nm IONPs with T_1 or dual T_1–T_2 MRI contrast enhancing capabilities, magnetic particle imaging applications that are dependent on specific IONPs and multifunctional IONPs for use in hybrid MRI.

In the final article, Steven J. Oldenburg, Ph.D. (nanoComposix, USA) provides an overview of lateral flow diagnostic assays. The author discusses the use of ultra-bright reporter particles based on the unique optical properties of gold nanoshells that significantly increase the sensitivity of lateral flow immunoassays.

Each article in this publication is accompanied by a list of relevant Sigma-Aldrich materials available from MilliporeSigma/Merck. For additional product information, visit us at **SigmaAldrich.com/matsci**. Please bother us with your new product suggestions, as well as thoughts and comments for *Material Matters*™ at **SigmaAldrich.com/technicalservice**.

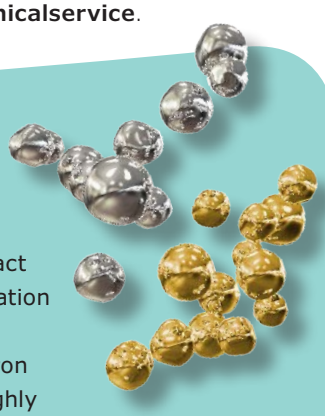

About the Cover

The unique optical and magnetic properties of nanomaterials, coupled with their ability to interact with cellular components, has fueled rapid innovation in biotechnology. As depicted in this cover art, functionalized metallic nanoparticles, magnetic iron oxide nanoparticles and quantum dots enable highly sensitive and specific new assay and detection platforms, diagnostic assays, bioimaging and even therapeutic treatments.

Merck KGaA, Darmstadt, Germany
Frankfurter Strasse 250
64293 Darmstadt, Germany
Phone +49 6151 72 0

To Place Orders / Customer Service
Contact your local office or visit
SigmaAldrich.com/order

Technical Service
Contact your local office or visit
SigmaAldrich.com/techinfo

General Correspondence
Materials Science
materialsscience@sial.com

Subscriptions
Request your FREE subscription to *Material Matters*™ at **SigmaAldrich.com/mm**

The entire *Material Matters*™ archive is available at **SigmaAldrich.com/mm**

Material Matters™ (ISSN 1933-9631) is a publication of Merck KGaA, Darmstadt, Germany

Table of Contents

Articles

Featured Products

Your Material Matters

Bryce P. Nelson, Ph.D.
Materials Science Initiative Lead

We welcome fresh product ideas. Do you have a material or compound you wish to see featured in our Materials Science line? If it is needed to accelerate your research, it matters. Send your suggestion to ***matsci@sial.com*** *for consideration.*

Dr. Jean-Paul (Moshe) Lellouche of Bar-Ilan University (Israel) recommended the addition of magnetic nanoparticles based on a γ-Fe_2O_3 maghemite core (**909211**) to our catalog. These particles are surface-doped using cerium ammonium nitrate to provide a highly positively charged, hydrophilic, and colloidally stable suspension of $Ce^{3/4+}$ cation/complex-doped nanoparticles. The maghemite nanoparticle cores are now available from Sigma-Aldrich with various shells and surface functionalization chemistries including branched polyethyleneimine (**909203**), oxidized branched polyethyleneimine (**909246**), branched polyethyleneimine & hyaluronic acid (**909238**), and branched polyethyleneimine & alginic acid (**909963**). Suspensions of 6–15 nm core/shell type NPs are super-paramagnetic,[1,2,3] fully biocompatible,[1,2] highly sensitive in MRI (T_2* contrast agent),[1,2] and enable successful coordinative attachment of therapeutic agents.[1,3] These unique attributes make these core-shell type cerium-doped iron oxide (III) nanoparticles well-suited for the development of effective drug and gene carriers.[1,2,3]

References

(1) Israel, L. L.; Lellouche, E.; Kenett, R. S.; Green, O.; Michaeli, S.; Lellouche, J.-P. *J. Mater. Chem. B* **2014**, *2* (37), 6215–6225.
(2) Lellouche, J.-P.; Michaeli, S.; Israel, L.L.; Lellouche, E.; Kapilov-Buchman, Y. Magnetic Inorganic Iron-Based Nanoparticles. WO/2014/147608 PCT/IL2014/050064, September 26, **2014**.
(3) Israel, L. L.;Lellouche, E.; Ostrovsky, S.; Yarmiayev, V.; Bechor, M.; Michaeli, S.; Lellouche, J.-P. *ACS Appl. Mater. Interfaces* **2015**, *7* (28),15240–15255

Name	Description	Cat. No.
Cerium doped iron oxide	3.2 mg/ml in H_2O	**909211-2ML**
	branched polyethyleneimine shell	**909203-2ML**
	branched polyethyleneimine and alginic acid shell	**909963-2ML**
	branched polyethyleneimine and hyaluronic acid shell	**909238-2ML**
	oxidized branched polyethyleneimine shell	**909246-2ML**

MilliporeSigma

THE FUTURE OF BIOIMAGING

Nanomaterial Bioconjugation Techniques

A guide for surface modification allowing bioconjugation of inorganic nanomaterials having applications in theranostics. Discover the latest advances and protocols in nanoparticle conjugation for:

- Magnetic Imaging
- Fluorescence Imaging
- Optical-based Imaging

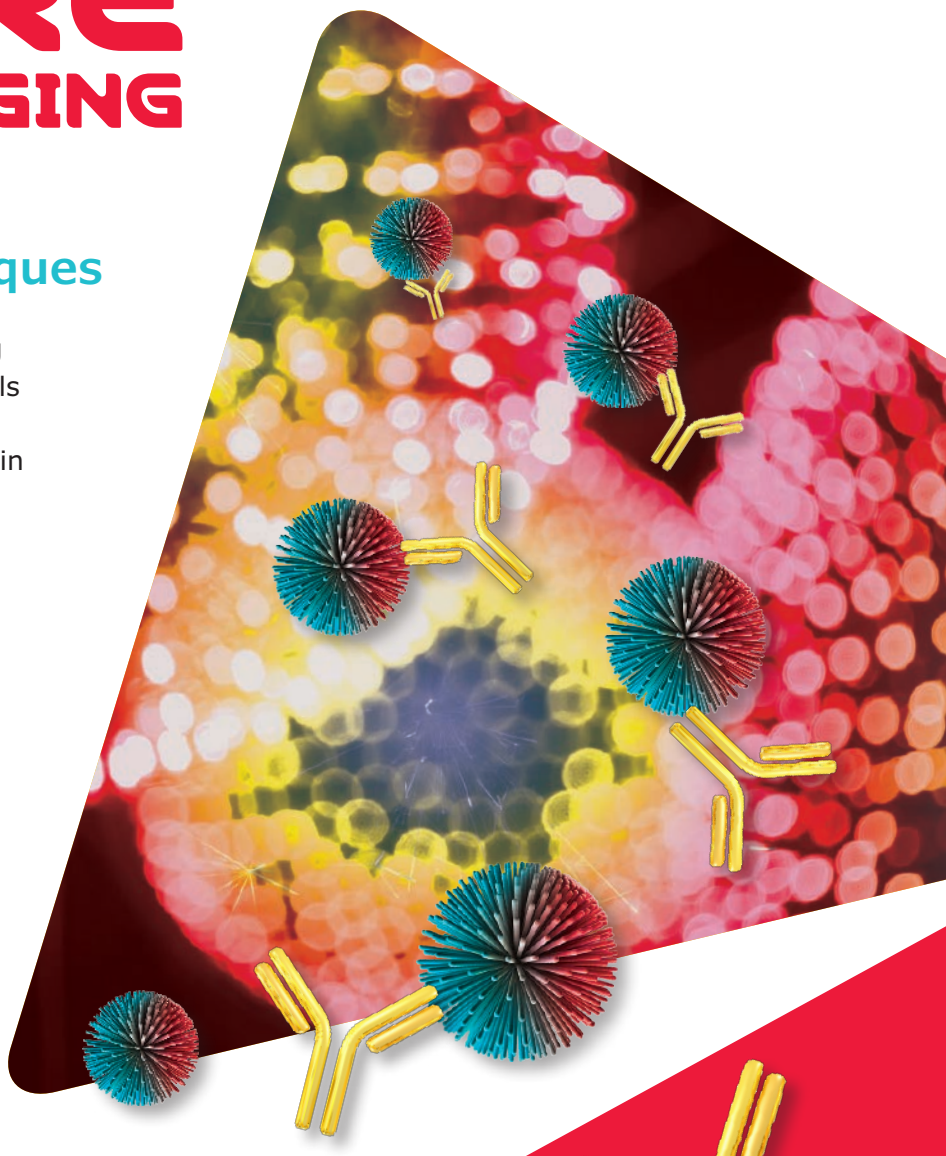

Order your complimentary copy from:
SigmaAldrich.com/nanomaterials-conjugation

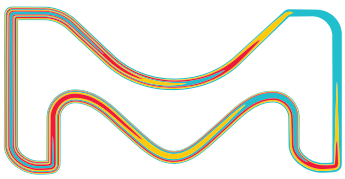

Sigma-Aldrich®
Lab & Production Materials

Applications of Quantum Dots in Bioimaging and Bioassays

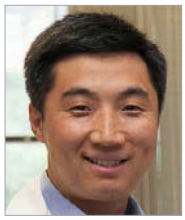

Robert H. Pierce[1] and Xiaohu Gao[2*]

[1]Program in Immunology, Fred Hutchinson Cancer Research Center, 1100 Fairview Ave N, Seattle, WA 98109, USA
[2]Department of Bioengineering, University of Washington, 3720 15th Ave NE, WA 98195, USA
*Email: xgao@uw.edu

Introduction

A detailed understanding of the dynamics of intercellular communication and intracellular signaling networks is highly sought-after by researchers involved in cell biology, pathology, clinical diagnostics, and drug discovery. Untangling and managing the complex interactions underlying cancer, neurological diseases, and immune system disorders are of particular interest because of their potential to unlock cures. Investigation of these biological processes requires affordable analytical tools with high-resolution, high-sensitivity, and the capability to perform multiplexed analysis. Fluorescent probes such as organic fluorophores simultaneously offer many of these features, and are at the core of many fundamental discoveries. At the same time, with more and more genomic, transcriptomic, and proteomic work identifying distinct biological processes, the level of complexity is increasing beyond the capability of conventional fluorophores, hampering the development of diagnostic kits and new therapeutics targeting key molecular mechanisms of pathogenesis.

Quantum dots (QDs), emerged as a result of the explosion in nanotechnology research conducted during the past three decades, offer a promising solution for researchers in need of more capable bioassay and bioimaging technologies. In terms of optical properties, QDs are superior in almost every aspect to organic dyes (**Table 1**). Their narrow and size-tunable light emission makes them ideal for multiplexed imaging. The Gaussian-shaped emission peaks with a full-width-at-half-maximum (FWHM) of approximately 20 nm allow 5 to 10 colors to fit into the visible spectrum alone, free of spectral overlap (or at least resolvable by spectral imaging).[1] The narrow emission of QDs is complemented by efficient light absorption over a broad spectral range (hundreds of nanometers), enabling simultaneous excitation of multiple colors by a single light source. This feature not only reduces the cost of imaging instrumentation (e.g., filter design) and simplifies data analysis (e.g., fluorescence intensity compensation), but also improves imaging sensitivity, as it can create a large Stokes shift away from the biological sample autofluorescence. QD fluorescence can also be differentiated from background autofluorescence using a gating approach that takes advantage of the long excited-state lifetime of QDs, which is approximately an order of magnitude longer than those of organic dyes. Although in theory the long lifetime could reduce the photon production rate (and consequently probe brightness), most biological imaging applications operate under absorption-limited conditions rather than lifetime-limited conditions, which require a very high excitation photon flux. Therefore, QDs with much higher molar extinction coefficients are found to be brighter probes than organic dyes. For organic dyes and QDs with similar quantum yields, individual QDs are generally 1–2 orders of magnitude brighter than dye molecules. In addition, QDs are significantly more resistant to photobleaching, well-suited for long-term imaging, and tracking applications.

Table 1. Comparison of organic dye and QD optical properties significant for bioapplications

Optical property	Conventional organic dyes	QDs
Absorption spectrum	Narrow in general	Broad and gradually increasing towards shorter wavelength
Emission spectrum	Broad with long-wavelength tails	Narrow, symmetrical, Gaussian distributed
Molar extinction coefficient	10^4–10^5 $M^{-1}cm^{-1}$	10^5–10^6 $M^{-1}cm^{-1}$ at the first exciton peak, increasing towards shorter wavelength
Quantum yield	High-quality dyes and QDs share similar quantum yields	
Fluorescence excited state lifetime	Nanoseconds	10 s nanoseconds
Photostability	Poor, rapid photobleaching	Highly stable
Stokes shift	Small in general, often <50 nm	Flexible depending on excitation wavelength, can be as large as 100s nm
Size	Small, ~1 nm	Large, core particle often 2–10 nm in diameter; polymer coating adds ~3 nm for the hydrodynamic size

QD Developments

Despite the remarkable optical properties, the synthesis and engineering of QDs have taken a long time to develop to the point where QDs became practical to use in biological imaging and bioassays. Since the initial discovery and establishment of quantum mechanical models for QDs in the early 1980s,[2–4] high-quality QDs only became commercially available after nearly 20 years of development.[5] The long development time period for QDs can broadly be divided in three major milestones: QD core synthesis, QD shell synthesis, and QD surface functionalization.

In 1993, Bawendi and co-workers[6] first reported a new route to synthesize monodisperse QD core particles. Deviating from the then-popular aqueous solution-based reactions, this approach instead used high temperature, organometallic reactants, and organic solvents. These conditions enabled rapid crystal nucleation and created a precise control between the competing processes of Ostwald ripening and molecular addition during nanocrystal growth.[7] As a result, this approach not only produced highly crystalline, uniform II-VI QDs of specific sizes, but also became the basic framework for the synthesis of other monodisperse nanoparticles, including III-V semiconductor, magnetic, metallic, and perovskite nanoparticles.[8–12]

However, QDs synthesized using Bawendi's method often suffered from quantum yields of less than 10%, severely limiting production of bright imaging probes. Due to the small particle size, a large percentage of the atoms were on the QD surface. These surface atoms created crystal defects that trapped charge carriers, thus preventing exciton recombination and fluorescence emission. A simple yet transformational solution was first reported by Hines and Guyot-Sionnest in 1996,[13] in which a thin shell was grown on top of the core nanoparticles. The shell was comprised of another semiconductor with a similar crystal lattice and higher energy bandgap. It effectively passivated the core particle surface and confined excitons to the core, thus promoting recombination and fluorescence emission. The initial core-shell QDs reached quantum yields of 30-50%; this was later improved to 80-90% through the use of more complex shells.[14]

The third technical milestone required to make QDs useful for biomedical applications was surface functionalization. High-quality QDs synthesized in organic solvents have a layer of hydrophobic surface ligands, which are incompatible with biological systems. Initial attempts to make QDs water-soluble were based on ligand exchange and silica coating, but both methods displaced the hydrophobic surface ligands[15,16] that were important for QDs' optical properties. In addition, water-soluble QDs prepared using these methods did not form stable colloids. Freshly synthesized QDs could be used in lab research for proof-of-concept studies but were unsuited for commercial applications. A number of labs explored amphiphilic polymers to make QDs water-soluble while retaining the hydrophobic ligands on their surface.[17–20] These polymers solubilize hydrophobic QDs much like the way detergent molecules wrap around tiny oil droplets. For example, Bruchez and coworkers at Quantum Dot Corporation developed a polymer with multiple repeats of hydrocarbon chains and polar head groups (e.g., carboxylic acids).[20] The hydrocarbon chains interdigitated into the hydrophobic surface ligands on the QD surface, whereas the polar head groups made the QDs water-soluble (**Figure 1**). This successful strategy soon became the base structure for most commercially available QD bioconjugates.

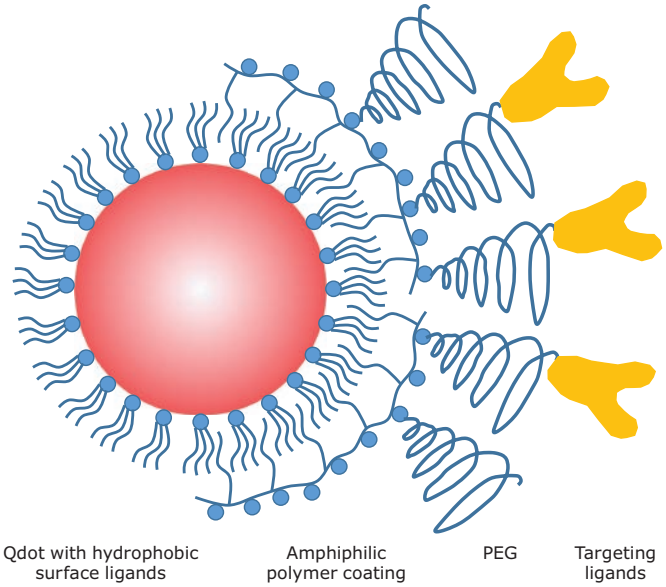

Figure 1. Schematic drawing of a common QD probe featuring a core particle capped by a layer of hydrophobic ligands, an amphiphilic encapsulating polymer layer for solubility, a polyethylene glycol (PEG) layer for non-specific binding reduction, and a targeting ligand for biomolecular recognition.

QD Bioapplications

The bioapplications of QDs can also be categorized into three general groups: sensing and detection, *in vitro* labeling and imaging, and *in vivo* imaging. For sensing and detection, an optical readout is used in both homogeneous assays (solution-based detection) and heterogeneous assays (assays on solid supports). The advantage of using QDs lies in their ability to improve the detection sensitivity by virtue of their unique optical properties including brightness and a large Stokes shift. One of the earliest QD biosensors based on fluorescence resonance energy transfer (FRET) was developed by Medintz, Mattoussi and Mauro.[21] In this system, recombinant maltose-binding protein (MBP) with a C-terminal histag self-assembled onto the QD surface through chelation. A β-cyclodextrin-fluorescence quencher conjugate bound in the MBP saccharide-binding site causes initial quenching of the QD fluorescence, whereas the presence of maltose capable of displacing the β-cyclodextrin-quencher conjugate restores QD fluorescence for detection. A disadvantage of using QDs in FRET assays is their physical size, as well as the surface coating materials, especially for highly stable amphiphilic polymer-coated QDs. These physical barriers increase the distance between energy donors and acceptors, thus reducing FRET efficiency. Fortunately, the reduced efficiency can be overcome using the tunable emission and large surface area of QDs, which allow optimization of spectral overlaps between donors and acceptors and immobilization of multiple energy acceptors per QD, respectively.[22] Furthermore, combining QD-based FRET probes with microfluidic devices can enable separation-free, single molecule-level (<50 copies) detection of target DNA sequences. This is possible because the confinement of multiple oligonucleotide probes on the QD surface captures and concentrates multiple target molecules on the same QD.[23]

The second popular application of QDs is fluorescent labeling and imaging. QDs can be conjugated to targeting ligands including small molecules, antibodies, peptides, and oligonucleotides. These conjugates can then be used to label target molecules immobilized in paper strips, membranes, biochips, gels, or cells. Molecular recognition is achieved by specific interaction between a target molecule and its ligand (e.g. antigen and antibody, and complementary DNA strands), and the target location and abundance are revealed by fluorescence. For example, immunohistochemistry (IHC) has been a workhorse for biological research and clinical diagnosis for more than 50 years. Conventional organic dye-labeled antibodies (or antibody labeling kits) are broadly available, but they suffer from a number of limitations. First, only 2–3 colors of organic dyes can be used in parallel, due to spectral overlap. Second, it is difficult to accurately quantify fluorescence signals because dye molecules quickly photobleach. Third, biological samples such as cells and tissues often have high background signals (autofluorescence) that interfere or even obscure spatially specific labeling. QDs conjugated to primary antibodies address all these problems. Single QD-antibody conjugates are sufficiently small to diffuse into properly fixed cells. Indeed, a number of research groups have demonstrated routine multicolor imaging of cell-surface, cytoplasmic, and nuclear antigens.[1,20,24-26]

Despite these advantages, QDs are not yet the primary choice for fluorescence labeling largely for two reasons. First, the multiplexing capabilities of QDs only improves staining from 2–3 colors to 5–10, still far below the level necessary for comprehensive molecular profiling. Second, although QD-antibody conjugation protocols have been well-optimized and developed,[27] they are labor-intensive, making it costly to produce a large library of conjugates.

Recently, we developed a multicolor, multicycle, molecular profiling (M3P) technology that addressed both problems.[28,29] To expand the multiplexing capability, we combined 5–10 color QD-antibody conjugates in a single cocktail, and incubated the mixture with cells or tissue sections to demonstrate parallel multiplexed staining (**Figure 2**). Following fluorescence microscopy, the stains were removed and the sample was regenerated for another round of multicolor staining. We have developed protocols for complete destaining of the cells with no signal carryover and without affecting cell morphology or biomarker antigenicity, thus allowing the next full cycle of

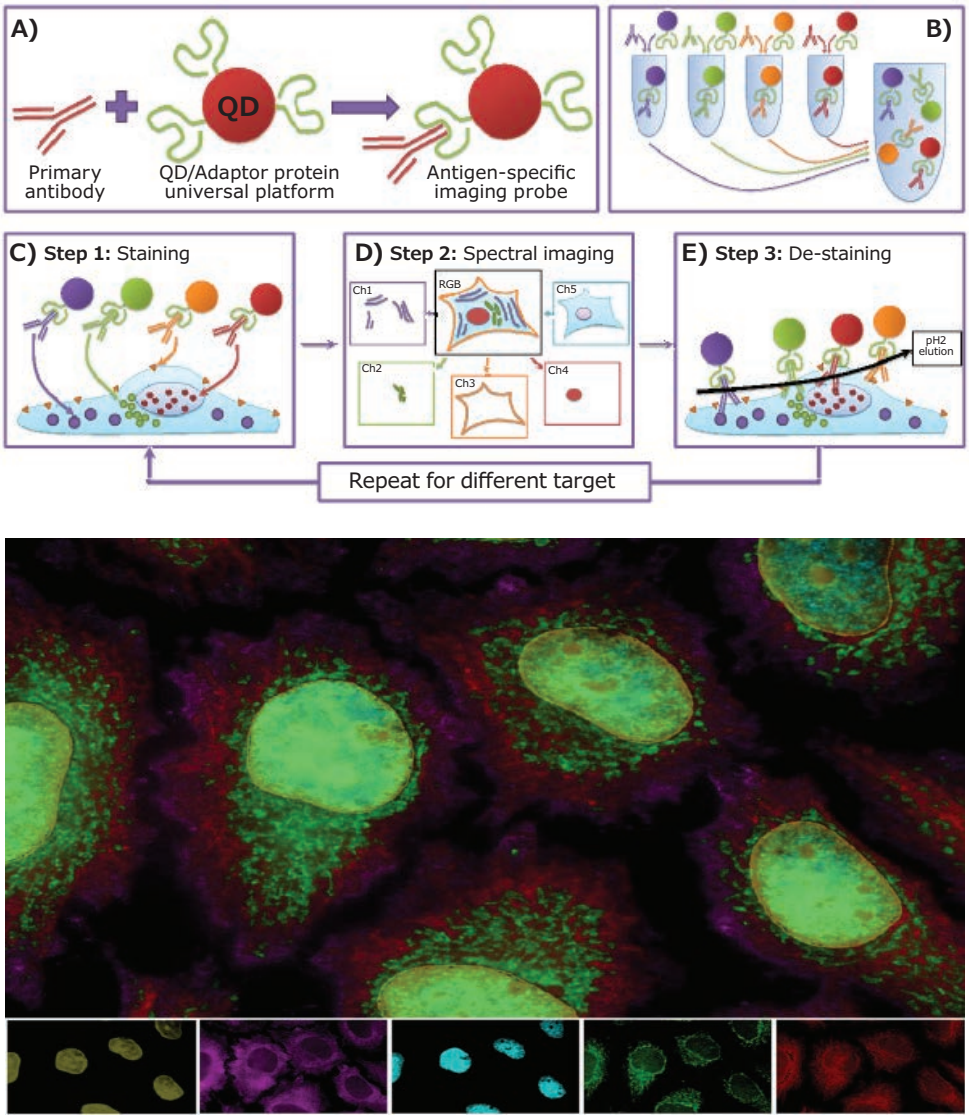

Figure 2. M3P technology enabling simple custom probe preparation and highly multiplexed single cell imaging. Key steps involve **A**) a universal QD-adaptor protein platform for single-step purification-free assembly of QD-antibody, **B**) mixing of multicolor QD probes into a single cocktail, **C**) parallel multiplexed staining, **D**) multicolor imaging, and **E**) destaining for another staining cycle. Bottom panel shows a representative fluorescence image of 5-target staining in Hela cells. Images adapted with permission from reference 28, copyright 2013 Nature Publishing Group.

IHC staining to identify a different subset of biomarkers. With each staining cycle, 10 biomarkers can be analyzed, using 10 spectrally distinct QDs. Performing IHC staining for 10 sequential cycles generates 10 subsets of data for the specimen, yielding an overall molecular profile consisting of 100 distinct biomarkers.

To reduce the labor required to make custom QD-antibody bioconjugates, we replaced the low-yield covalent QD-antibody conjugation with a non-covalent self-assembly protocol joining a universal QD-protein A platform with a variety of intact primary antibodies. The method requires no chemical reactions or purifications for end users, and enables quick and easy preparation of custom QD-antibody panels at extremely small scale (**Figure 2A**). The non-covalent interaction between the adaptor protein and primary antibodies is sufficiently stable during staining, and does not cross react. Therefore, the M3P technology enables extensive molecular characterization of cells within their native microenvironment in just a few cycles, making QDs practically useful for highly multiplexed IHC.

The third category of QD bioapplications is *in vivo* imaging. Dubertret et al.[17] reported the first use of QDs in a living organism, a frog embryo. The chemical- and photo-stability of QDs allowed cell lineage tracking and comparative embryology studies for up to four days, without abnormalities in embryo development. For *in vivo* targeting, Akerman et al.[30] showed that QDs guided by peptides concentrated at tumor blood vessels using *ex vivo* histology sections. Gao and coworkers first demonstrated non-invasive tumor imaging in mice using QD-antibody conjugates.[18] Hyperspectral imaging was used

to help delineate QD fluorescence from background because mouse skin autofluorescence was still high even when red QDs (relatively long wavelength with large Stokes shift) were used to make the targeted imaging probe. For improved light penetration depth and reduced autofluorescence, Kim et al.[31] prepared another type of QD in which the core valence and conduction band edges were both lower or higher than those of the shell. This arrangement effectively red-shifted QD emission to the near infrared (NIR) region, at the cost of exciton recombination rates. These NIR QDs were injected in mice and pigs intradermally, where they quickly drained to nearby lymph nodes, allowing image-guided surgery.

Perspectives

The spectral rainbow enabled by QD technology and the science behind it are both beautiful and fascinating. Ever since QDs were first used in cell staining, they promised a quantum leap for bioassay and bioimaging. Realization of that promise, however, has been delayed by a number of technical hurdles. As a result, QDs struggled to become a robust tool for real biological discoveries over the past 20 years. The vast majority of QD bioapplications to date involve technology developments or proof-of-concept use in model systems. With most of the technical issues addressed recently, identification of killer applications for QDs (significant biological problems that conventional dyes are inadequate for), will be a focus in the coming years. Mutlicolor, quantitative biomarker imaging such as immunofluorescence and fluorescence *in situ* hybridization in cells and tissues remains an exciting area of research and development. For example, in immunotherapy research, highly multiplexed molecular profiling of the cell genome, transcriptome, and proteome within a native microenvironment is expected to reveal new secrets of the complex and dynamic human immune system. Understanding the molecular, cellular, and organismal interactions requires high-throughput and high-content molecular analysis tool kits. QDs can aid the development of immunotherapies that one day may transform the lives of people affected by various immune diseases.

For *in vivo* applications, QD probes are expected to have an immediate impact on small animal imaging. In preclinical studies of drug discovery, for example, QDs offer significant advantages over current imaging modalities (e.g., MRI and PET), simultaneously achieving high sensitivity, high resolution, and low cost. In addition, QDs are an ideal prototype material for nanoparticle engineering. A great deal of information including the effects of particle size, shape, charge, surface coating, and targeting ligand, can be learned using QDs, and then applied to the design of other types of nanomaterials.

The prospects for the *in vivo* use in human diagnostics and theranostics remains unclear. Any application of QDs in humans must provide benefits that significantly outweigh the risks, and this remains to be shown. One fundamental limitation of optical imaging is that light does not penetrate deeply through tissues; QD toxicity is also a concern. The light penetration hurdle could potentially be overcome by advanced endoscopy technologies.

In summary, recent advances in both chemistry and colloidal science have made QDs a robust and readily available imaging tool. Following their commercial success in display technologies, widespread application of QDs in life science are not far behind. The unique optical properties of QDs complement those of conventional organic dyes and fluorescent proteins and will enable new discoveries in many unexplored or underexplored areas in biology. The future for QDs is bright.

References

(1) True, L. D.; X. Gao, *J. Mol. Diagn.* **2007**, *9* (1), 7–11.
(2) Brus, L. E.; *J. Chem. Phys.* **1984**, *80* (9), 4403–4409.
(3) Rossetti, R.; Nakahara, S.; Brus, L.E. *J. Chem. Phys.* **1983**, *79* (2), 1086–1088.
(4) Efros, A. L.,. Efros, A. L. *Semiconductors* **1982**, *16* (7), 772–775.
(5) Jovin, T. M. *Nat. Biotechnol.* **2003**, *21*, 32.
(6) Murray, C. B.; Norris, D. J.; Bawendi, M. G. *J. Am. Chem. Soc.* **1993**, *115* (19), 8706–8715.
(7) Peng, X.; Wickham, J.; Alivisatos, A. P. *J. Am. Chem. Soc.* **1998**, *120* (21), 5343–5344.
(8) Protesescu, L.; et al. *Nano Lett.* **2015**, *15* (6), 3692–3696.
(9) Battaglia, D.; Peng, X. *Nano Lett.* **2002**, *2* (9), 1027–1030.
(10) Park, J.; et al. *Nat. Mater.* **2004**, *3*, 891.
(11) Park, J.; et al. *Angew. Chem.* **2005**, *44* (19), 2872–2877.
(12) Puntes, V. F.; Krishnan, K. M.; Alivisatos, A. P. *Science* **2001**, *291* (5511), 2115–2117.
(13) Hines, M. A.; Guyot-Sionnest, P. *J. Phys. Chem.* **1996**, *100* (2), 468–471.
(14) Xie, R.; et al. *J. Am. Chem. Soc.* **2005**, *127* (20), 7480–7488.
(15) Bruchez, M.; et al. *Science* **1998**, *281* (5385), 2013–2016.
(16) Chan, W. C. W.; Nie, S. *Science* **1998**, *281* (5385), 2016–2018.
(17) Dubertret, B.; et al. *Science* **2002**, *298* (5599), 1759–1762.
(18) Gao, X.; et al. *Nat. Biotechnol.* **2004**, *22*, 969.
(19) Pellegrino, T.; et al. *Nano Lett.* **2004**, *4* (4), 703–707.
(20) Wu, X.; et al. *Nat. Biotechnol.* **2002**, *21*, 41.
(21) Medintz, I. L.; et al. *Nat Mater.* **2003**, *2*, 630.
(22) Medintz, I. L.; et al. *J. Am. Chem. Soc.* **2004**, *126* (1), 30–31.
(23) Zhang, C. -Y.; et al. *Nat Mater.* **2005**, *4*, 826.
(24) Ghazani, A. A.; et al. *Nano Lett.* **2006**, *6* (12), 2881–2886.
(25) Giepmans, B. N. G.; et al. *Nat. Methods* **2005**, *2*, 743.
(26) Yezhelyev, M. V.; et al. *Adv. Mater.* **2007**, *19* (20), 3146–3151.
(27) Zrazhevskiy, P.; Dave, S. R.; Gao, X. *Part. Part. Syst. Charact.* **2014**, *31* (12), 1291–1299.
(28) Zrazhevskiy, P.; Gao, X. *Nat. Commun.* **2013**, *4*, 1619.
(29) Zrazhevskiy, P.;True, L. D.; Gao, X. *Nat. Protoc.* **2013**, *8*, 1852.
(30) Åkerman, M. E.; et al. *Proc. Natl. Acad. Sci.* **2002**, *99* (20), 12617–12621.
(31) Kim, S.; et al. *Nat. Biotechnol* **2003**, *22*, 93.

Cadmium-Free Quantum Dots

PbS

Name	Form	Description	Fluorescence Emission, λ_{em} (nm)	Cat. No.
PbS core-type quantum dots	10 mg/mL in toluene	oleic acid coated	900	**900733-5ML**
		oleic acid coated	1000	**747017-10ML**
		oleic acid coated	1100	**900735-5ML**
		oleic acid coated	1200	**747025-10ML**
		oleic acid coated	1300	**900737-5ML**
		oleic acid coated	1400	**747076-10ML**
		oleic acid coated	1500	**900728-5ML**
		oleic acid coated	1600	**747084-10ML**

$CsPb(Cl,Br)_3$-Based Perovskite Quantum Dots

Name	Form	Description	Fluorescence Emission, λ_{em} (nm)	Cat. No.
Perovskite quantum dots	10 mg/mL in toluene	oleic acid and oleylamine coated	450	**900748-5ML**
		oleic acid and oleylamine coated	480	**900747-5ML**
		oleic acid and oleylamine coated	510	**900746-5ML**

InP/ZnS

Name	Form	Description	Fluorescence Emission, λ_{em} (nm)	Cat. No.
InP/ZnS quantum dots	5 mg/mL in toluene	stabilized with oleylamine ligands	530	**776750-5ML**
		stabilized with oleylamine ligands	560	**776793-5ML**
		stabilized with oleylamine ligands	590	**776769-5ML**
		stabilized with oleylamine ligands	620	**776777-5ML**
		stabilized with oleylamine ligands	650	**776785-5ML**

Cadmium-Based Quantum Dots

Core-Type Quantum Dots

CdTe

Name	Form	Description	Fluorescence Emission, λ_{em} (nm)	Cat. No.
CdTe core-type quantum dots	powder	COOH functionalized	510	**777986-10MG** **777986-25MG**
		COOH functionalized	520	**777935-10MG** **777935-25MG**
		COOH functionalized	570	**777943-10MG** **777943-25MG**
		COOH functionalized	610	**777951-10MG** **777951-25MG**
		COOH functionalized	770	**777994-10MG** **777994-25MG**
		COOH functionalized	710	**777978-10MG** **777978-25MG**

Core-Shell Type Quantum Dots

CdS/ZnS

Name	Form	Description	Fluorescence Emission, λ_{em} (nm)	Cat. No.
CdS/ZnS core-shell type quantum dots	4 µM in PBS, dispersion	amine	400	**900290-250UL**
		amine	425	**900305-250UL**
		amine	450	**900304-250UL**
	1 mg/mL in H_2O, dispersion	carboxylic acid	400	**900298-1ML**
		carboxylic acid	425	**900299-1ML**
		carboxylic acid	450	**900294-1ML**
	lyophilized powder	carboxylic acid	400	**900310-1MG**
		carboxylic acid	425	**900308-1MG**
		carboxylic acid	450	**900332-1MG**
		oleic acid	400	**900280-10MG**
		oleic acid	425	**900283-10MG**
		oleic acid	450	**900282-10MG**
	5 mg/mL in toluene,	oleic acid	400	**900286-1ML**
		oleic acid	425	**900333-1ML**
		oleic acid	450	**900334-1ML**
	4 µM in H_2O, dispersion	PDDA coated	400	**900306-250UL**
		PDDA coated	425	**900307-250UL**
		PDDA coated	450	**900309-250UL**
		PEG	400	**900303-250UL**
		PEG	425	**900302-250UL**
		PEG	450	**900301-250UL**

CdSe/ZnS

Name	Form	Description	Fluorescence Emission, λ_{em} (nm)	Cat. No.
CdSe/CdS core-shell type quantum rods	5 mg/mL in hexane, dispersion	carboxylic acid	530	**900511-1ML**
		carboxylic acid	560	**900512-1ML**
		carboxylic acid	590	**900515-1ML**
		carboxylic acid	620	**900514-1ML**
CdSe/ZnS core-shell type quantum dots	solid	stabilized with octadecylamine ligands	520	**748021-10MG** **748021-25MG**
		stabilized with octadecylamine ligands	540	**748056-10MG** **748056-25MG**
		stabilized with octadecylamine ligands	560	**748080-10MG** **748080-25MG**
		stabilized with octadecylamine ligands	580	**748129-10MG** **748129-25MG**
		stabilized with octadecylamine ligands	600	**748099-10MG** **748099-25MG**
		stabilized with octadecylamine ligands	620	**790192-10MG** **790192-25MG**
		stabilized with octadecylamine ligands	630	**790206-10MG** **790206-25MG**

Alloyed Quantum Dots

Name	Form	Description	Fluorescence Emission, λ_{em} (nm)	Cat. No.
CdSeS/ZnS alloyed quantum dots	1 mg/mL in toluene	oleic acid	450	**753742-5ML 753742-25ML**
		oleic acid	490	**753750-5ML 753750-25ML**
		oleic acid	525	**753769-5ML 753769-25ML**
		oleic acid	540	**753777-5ML 753777-25ML**
		oleic acid	575	**753785-5ML 753785-25ML**
		oleic acid	630	**753793-5ML 753793-25ML**
		oleic acid	665	**753807-5ML 753807-25ML**
	1 mg/mL in H_2O,	COOH functionalized	490	**754226-1ML 754226-5ML**
		COOH functionalized	525	**753831-1ML 753831-5ML**
		COOH functionalized	540	**753866-1ML 753866-5ML**
		COOH functionalized	575	**753874-1ML 753874-5ML**
		COOH functionalized	630	**753882-1ML 753882-5ML**
		COOH functionalized	665	**753890-1ML 753890-5ML**
CdSeS/ZnS alloyed quantum dots kit	5 X 1 mg/mL in toluene	Size: 1 ml x 5 vials, oleic acid	490-665	**753823-1KT**
	5 X 1 mg/mL in H_2O	COOH functionalized	490-665	**753904-1KT**

Fluorescent Nanomaterials for Bioimaging: Considerations of Particle Brightness, Photostability, and Size

Philipp Reineck[1] and Marco Torelli[2]

[1]ARC Centre of Excellence for Nanoscale BioPhotonics & School of Science, RMIT University, Melbourne, VIC 3001, Australia
[2]Adámas Nanotechnologies, Inc., 8100 Brownleigh Drive, Suite 120, Raleigh, North Carolina, 27617, USA

Introduction

Fluorescence microscopy has become an essential component of many biological studies, affecting everything from fundamental research to clinical diagnostics. In contrast to other imaging methods such as electron microscopy, computed tomography, and ultrasound, fluorescence microscopy combines high spatial resolution with targeted, multispectral contrast.[1–2] While organic fluorophores and fluorescent proteins are vital tools in biology and biotechnology laboratories today, other fluorescent nanomaterials are increasingly being used in research laboratories around the world, in applications ranging from deep tissue imaging *in vivo*[3–4] to point-of-care diagnostics.[5] In contrast to the majority of organic fluorophores, which are under 1 nm in size, nanomaterials range from 1–100 nm in size, allowing them to act as discrete entities with a loadable surface. Fluorescent nanomaterials have achieved success in a variety of applications because of their beneficial capabilities which enable:

- High optical contrast in otherwise contrast-free samples
- Visualization or detection of specific components of complex biological systems
- Visualization of structures at high spatial and temporal resolutions — well below 100 nm size and millisecond timescales
- Quantification of physical (temperature, magnetic fields, strain) and biochemical properties (pH, concentration of molecules and ions) down to the subcellular level
- Delivery of payloads in accord with targeting

Considering these benefits, an 'ideal' nanoparticle is shown in **Figure 1**. This ideal material would show high fluorescence brightness with high uniformity across different particles, no photo-bleaching, perfect biocompatibility, and highly selective binding to, or detection of, the specific analyte of interest. While these attributes are desirable in most applications, the ideal size of a nanomaterial strongly depends on the application and size of the objects of interest. While the perfect nanoparticle does not yet exist, great advancements have been made in the field. In this article, we will review current state-of-the-art materials, with an emphasis on fluorescence brightness, photostability, and size, and relate them to emerging applications.

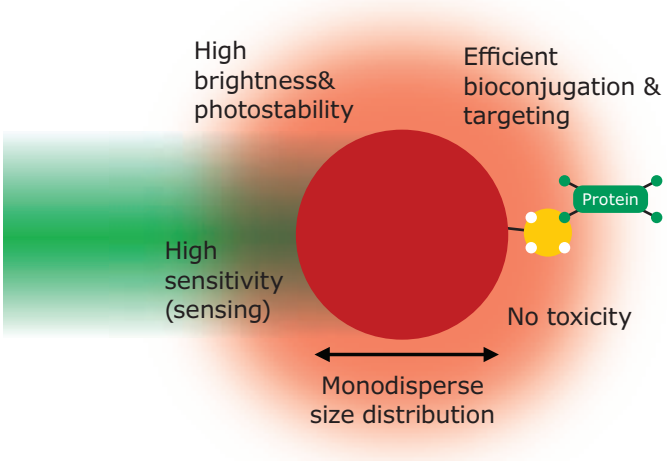

Figure 1. The properties of an 'ideal' fluorescent nanomaterial.

Brightness

Fluorescence brightness is a vital property of every fluorescent nanomaterial. Sufficient fluorescence brightness is critical to show a signal against the often autofluorescent background found in biological systems. The fluorescence brightness, B, is generally defined as the product of absorption coefficient (ε) and quantum yield (Γ): $B = \varepsilon \Gamma$. A bright material must emit absorbed excitation light efficiently, i.e. it must have a high fluorescence quantum yield. It must also absorb photons efficiently, which is to say it needs a high absorption coefficient. The latter is often quantified in terms of moles, for example [$M^{-1}cm^{-1}$], meaning that the physical size of the material is not taken into account. However, size is an important parameter. Organic dyes are usually about 1 nm in diameter, about 10 to 100 times smaller than most fluorescent nanoparticles. A semiconductor-based quantum dot (QD) may absorb light 10 times more efficiently than an organic dye, but its volume is also often more than 100 times larger! Therefore, the answer to the question "Which material is brighter?", often rests on whether the comparison is made based on molecule/particle numbers (and a molar extinction coefficient) or on the materials' mass (and a mass-based extinction coefficient).[6] These two measures of brightness are compared for six different types of nanomaterials in Table 1. The molar brightness of molecular fluorophores like fluorescein and green fluorescent protein (GFP) is surpassed by several materials. However, due to the small size of molecules like fluorescein, their mass brightness exceeds those of other molecules more than an order of magnitude.

Table 1. Comparison of the molar and mass-based fluorescence brightness of selected fluorescent nanomaterials. Mass-based brightness values are estimated, based on molecular weight, particle sizes, and densities.

Material	Size [nm]	Molar brightness $M^{-1}cm^{-1}$	Mass brightness $(g/L)^{-1}cm^{-1}$	References
Fluorescein	<1	72,000	215	**11**
Green fluorescent protein	~3	33,000	1.2	**12**
Carbon dot	3	4,000	0.2	**13**
CdSeS/ZnS quantum dot	6	240,000	1.1	**6**
Polymer dot	10	3,000,000	10	**14**
Nanodiamond	100	1,700,000	0.002	**15**

A single 100 nm nanodiamond or 10 nm polymer dot exceeds the brightness of a fluorescein molecule by more than one order of magnitude, but at the cost of a larger particle size. However, larger particles are not always bad, and sometimes even required from a biological standpoint — for example to evade immediate clearance in an *in vivo* experiment. The detection of rare events, where the unambiguous detection of individual particles is paramount, can also be enhanced by the extremely high molar brightness of larger particles (also see section on 'Size'). Generally, mass brightness is skewed towards small and low-density materials; for example carbon dots exhibit a reasonable mass brightness, but their molar brightness is much less than that of other materials. Molar brightness has its origin in the world of molecules, and ignores the size of nanoparticles. Practically, selecting the most meaningful measure of brightness depends on the specific particle and application of interest.

In general, organic dyes absorb light very efficiently, because the entire molecule interacts with light through delocalized electrons. Nanodiamonds, on the other hand, mostly consist of a transparent diamond matrix, which only contains about 0.001% by weight of so-called "color centers," like nitrogen-vacancy (NV) centers, which absorb light and fluoresce.[7] Hence, the potential for improvement is enormous. The extinction and brightness of semiconductor quantum dots and polymer dots increases with their increasing size.[8,9] Nanodiamonds are one of the few materials whose brightness has the potential to be increased significantly by improving the quality of NV centers. Work is in progress to develop gentle methods of micron-sized particle fragmentation or use bottom-up synthesis of particles containing NV centers.[10]

Photostability

Most applications involve multiple cycles of nanomaterial excitation and collection of the fluorescence signal. Even in the simplest *in vitro* cellular imaging experiment, when only a few images are required, finding a region of interest usually requires at least several seconds of light excitation. Therefore, photostability is an important parameter — the brightest fluorescent material is useless if the intensity fades too quickly. This phenomenon of fading is called "photobleaching." The physiochemical changes involved in the process of photobleaching are often complex, highly material specific, and highly dependent on the local environment and the intensity of light excitation used. Many materials can exhibit either high or low photostability, depending on the particular environment and illumination intensity used. This partially explains the lack of quantitative information on the photostability of fluorescent nanomaterials in the scientific literature. Some widely known and used fluorophores, such as fluorescein, have been investigated in great detail,[16-17] but most newer materials have not.

Two common measures of photostability are 1) absolute or lifetime photostability — the average number of photons a fluorophore can emit before becoming inactive and 2) photobleaching rate — the decrease in fluorescence intensity per unit of time. Absolute photostability is independent of excitation intensity over a wide range, but is experimentally challenging to measure. The photobleaching rate can be determined more readily, but is highly dependent on illumination intensity.

The fluorescence intensity as a function of time for several fluorescent nanomaterials suspended in water and imaged under a commercial wide-field fluorescence microscope is shown in **Figure 2**.[4] Illumination intensities on the order of 10 W cm^{-2} were used, which are very moderate relative to the excitation intensities commonly used in confocal microscopy (10–100 W cm^{-2}), up conversion nanoparticle imaging (100–1000 W cm^{-2}),[18] and stimulated emission depletion super-resolution imaging (>1000 W cm^{-2}).[19] For example, Alexa 647 is a common red fluorophore that shows a characteristic photobleaching time (the inverse of the photobleaching rate) of about 8 seconds under these conditions. In contrast, nanodiamonds show no photobleaching at all, and drift in the excitation intensity is actually the highest source of variability. All other materials show photobleaching characteristics between these two extremes. In practice, brightness and photostability are closely related: a brighter material can be excited at lower light intensities and thus achieve the same image contrast as a less bright fluorophore. Therefore, the appropriate measure of photostability is also application dependent. **Figure 2** only shows one possible scenario, where equal excitation intensities are used.

Size of Fluorescent Nanoprobes

Nanomaterial size is an important parameter that largely determines how a biological system interacts with the exogenous material. Size affects both active and passive cell uptake, active and passive transport processes, immune system responses, clearance pathways, and toxicity, to name some important examples.[20] It also plays an important part in physical and chemical processes including diffusion, ionic interactions, and chemical bond formation. As with the previous characteristics, ideal particle size strongly depends on the application.

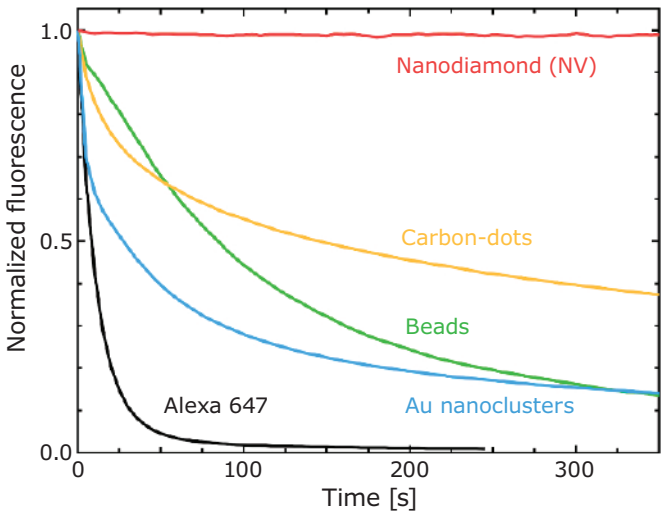

Figure 2. Photostability of several fluorescent nanomaterials in a wide-field fluorescence microscopy experiment. All materials were dispersed in deionized water and illuminated with excitation intensity of ~10 W cm^{-2}. Reproduced with permission from reference 6, copyright 2016 Wiley.

In complex biological environments such as blood, serum, or even growth media, the formation of a protein corona makes the determination of the nanoparticle size highly non-trivial.[20] High concentrations of salts (~100 mM) and highly charged small molecules (including amino acids) in many of these environments can cause strong nanoparticle aggregation, which further complicates the size analysis and often causes 'size' to fluctuate over time.[21]

Table 2 summarizes some general considerations regarding the suitability of nanomaterials in particular size ranges for different applications and research requirements. In order to investigate the dynamics of a system, the size of the fluorescent nanomaterial being used relative to the objects involved in the process must be considered. For example, in order to study the dynamics of individual molecules, only the smallest fluorescent labels can be employed, since the inertia of larger nanoparticles will interfere with or even halt entirely most of these processes. On the other hand, if intracellular transport along microtubules is the focus of the inquiry, nanoparticles up to tens of nanometers may be a good choice, since individual nanoparticles can provide higher contrast (and therefore potentially higher temporal resolution) and higher photostability. Eukaryotic cells routinely transport larger objects such as vesicles and parts of organelles via motor proteins, and a 30 nm nanoparticle may only have a minor effect on the transport dynamics.[22] Moreover, size can directly influence the cellular uptake of particles.[23]

Table 2. Main nanomaterials size regimes for biomedical applications.

Application / Requirement	Ideal nanomaterial size
Molecular dynamics	<1 nm
Good clearance *in vivo*	<5 nm
Single particle tracking	<100 nm
Targeting *in vivo*	150–250 nm

In experiments *in vivo*, the interactions are often even more complex and less well-understood. In fact, there is agreement in the scientific community on only a few aspects of nanomaterial size effects. Renal clearance of nanomaterials generally requires a hydrodynamic radius (including adsorbed biological species) below 5.5 nm.[24] Particles up to ~200 nm are cleared by the liver, while larger particles are filtered by the spleen.[25] Particles on the order of ~150 nm are thought to be optimal to avoid clearance by the spleen and increase targeting potential due to their longer circulation time.[26]

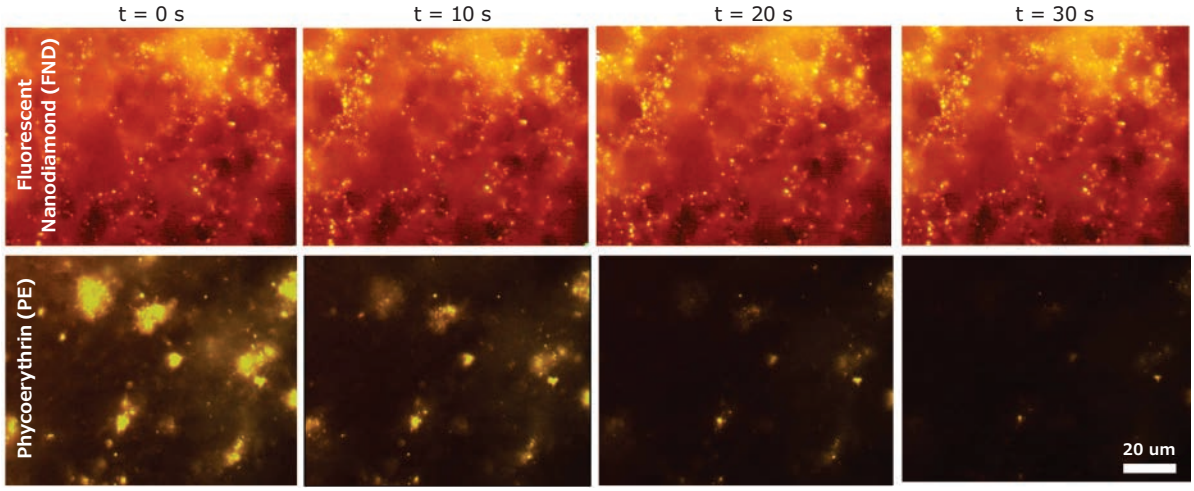

Figure 3. Time-lapse of blood clots incubated with a biotinylated platelet activation antibody (anti-CD41-biotin), incubated with streptavidin conjugated to either fluorescent nanodiamond (**top**) or phycoerythrin (PE) (**bottom**). PE quickly degrades, while the fluorescent nanodiamond (FNDs) signal remains constant.

Applications

One current application of photostable fluorophores is to follow biological phenomena over time via long-term imaging.[27] This can allow cell tracking[28] and whole organism imaging over several days.[29] Figure 3 exemplifies how quickly the image quality can degrade at high magnification in an imaging experiment. While an initial image set is collected, it is fundamentally difficult to make fine adjustments to the field of view focus without sacrificing image quality. Emission in the near infrared (NIR) regime is also a critical factor for *in vivo* imaging.[30-31] Many nanomaterials (including quantum dots and nanodiamonds) have emission in the near-infrared (NIR). Potential *in vivo*[32] clinical applications include fluorescence image-guided surgery, when bleaching of the tumor marker can be suppressed.[32] The brightness of the tumor marker at tissue penetrating wavelengths is a critical factor for *in vivo* imaging.

Photostable nanomaterials are particularly important in emerging applications using high laser intensities, where photobleaching is a critical limiting factor. For instance, nanodiamond can withstand over 100 MW cm^{-2} intensity without bleaching.[34] In super-resolution imaging, which allows for image resolutions below the diffraction limit, photostability has both direct and indirect effects. Directly, fluorophores often need to withstand high excitation intensities for extended periods of time. Indirectly, since the resolution in stimulated emission depletion (STED) microscopy generally increases with increasing excitation power, the more photo stable a material is better.[35] Fundamentally, resolution is limited by the size of the particle,[36] though it is possible to image individual NV centers with resolution down to 6 nm.[37] Being able to withstand high laser intensities, nanodiamonds allow the highest possible image resolution.[38] In stochastic optical reconstruction microscopy (STORM) though not directly adding to cellular contrast, nanodiamonds serve as fiducial markers to correct for stage drift, thereby routinely allowing the acquisition of images with 10 nm resolution[39] (with as low as 2.6 nm[40] demonstrated) and up to 26 multiplex rounds — unprecedented for a super-resolution technique.[40]

In multiphoton microscopy, high resolution fluorescence images can be acquired as deep as hundreds of microns below the surface tissue. Multiphoton excitation enables tight focusing of light inside tissue, and allows for optical cross-sectioning and a reduction in background fluorescence.[41-42] While the excitation area may be reduced, high local laser intensities in the focal spot still cause photobleaching.[43-44] Two-photon excitation has been used to image fluorescent nanodiamond (FND) in MCF-7 breast cancer cells (at 800 nm excitation)[45] and HeLa cells, demonstrating a large contrast increase by reducing the background fluoresence.[46-47] For *in vitro* use, visualization of particles down to 40 nm in size has been shown.[47] In these examples, under high illumination conditions (up to 3 GW cm^{-2} and up to 10 min), no bleaching for two-photon emission was observed.[46,48]

Although we have highlighted examples where photostable materials shine, photobleaching itself can be used as an imaging technique. Historically, techniques such as fluorescence recovery after photobleaching (FRAP) has been used to determine molecular diffusion rates. Recently, photobleaching-assisted STORM improved the achievable signal-to-noise ratio of this technique, which is particularly useful for analytes with extremely high autofluorescence.[49] Moreover, photobleaching itself can be used as a contrast mechanism to allow for multiplexed imaging, when the different photobleaching times of various dyes can be used to provide contrast in a signal channel.[50]

Fluorescent nanomaterials often have other mechanisms of contrast as well, opening the possibility of multimodal imaging to increase both resolution and sensitivity. Fluorescent

nanomaterials may complement magnetic resonance,[51] electron micrscopy,[52] and computed tomography[53] imaging techniques in the future — even beyond scientific research laboratories and into operating theatres, for example.

Conclusion

The current generation of fluorescent nanomaterials is enabling significant advances in biological imaging. Selecting the best material for a specific application is a complicated decision, and many factors must be considered including a nanomaterial's brightness, photostability, biological safety, sensing ability, and size. The question "Which material is the best?" is obsolete, and should instead be "Which material is the best for my application?" Identifying the best material and adapting and optimizing all experimental processes to this material is not simple. As a result, many emerging materials have yet to be used to their fullest potential, and close collaborations between materials scientists and biologists are essential to bring this to fruition. There are several current fluorescent nanomaterials that exhibit unprecedented fluorescence brightness. Nanodiamond, however, shines brightest by offering genuine, unchanging resistance against photodegradation in combination with unique sensing capabilities.

References

(1) Falati, S.; Gross, P.; Merrill-Skoloff, G.; Furie, B. C.; Furie, B. *Nat. Med.* **2002**, *8*, 1175.
(2) Furie, B.; Furie, B. *J. Thromb. Haemost.* **2007**, *5*, 12–17.
(3) Miller, D. R.; Jarrett, J. W.; Hassan, A. M.; Dunn, A. K. *Curr. Opin. Biomed. Eng.* **2017**, *4*, 32–39.
(4) Reineck, P.; Gibson, B. C. *Adv. Opt. Mater.* **2017**, *5*, 1600446.
(5) Quesada-González, D.; Merkoçi, A. *Chem. Soc. Rev.* **2018**, *47*, 4697–4709.
(6) Reineck, P.; Francis, A.; Orth, A.; Lau, D. W. M.; Nixon-Luke, R. D. V.; Rastogi, I. D.; Razali, W. A. W.; Cordina, N. M.; Parker, L. M.; Sreenivasan, V. K. A. *Adv. Opt. Matter.* **2016**, *4*, 1549–1557.
(7) Shenderova, O.; McGuire, G. E. *Biointerphases* **2015**, *10*, 030802.
(8) Yu, W. W.; Qu, L.; Guo, W.; Peng, X. *Chem. Mater.* **2003**, *15*, 2854–2860.
(9) Sun, K.; Chen, H.; Wang, L.; Yin, S.; Wang, H.; Xu, G.; Chen, D.; Zhang, X.; Wu, C.; Qin, W. *ACS Appl. Mater. Interfaces* **2014**, *6*, 10802–10812.
(10) Alkahtani, M. H.; Alghannam, F.; Jiang, L.; Almethen, A.; Rampersaud, A. A.; Brick, R.; Gomes, C. L.; Scully, M. O.; Hemmer, P. R. *Nanophotonics* **2018**, *7*, 1423–1453.
(11) Sjöback, R.; Nygren, J.; Kubista, M. *Spectrochim. Acta Part A* **1995**, *51*, L7–L21.
(12) McRae, S. R.; Brown, C. L.; Bushell, G. R. *Protein Expr. Purif.* **2005**, *41*, 121–127.
(13) Castro, H. P.; Pereira, M. K.; Ferreira, V. C.; Hickmann, J. M.; Correia, R. R. *Opt. Mater. Express* **2017**, *7*, 401–408.
(14) Wu, C.; Jin, Y.; Schneider, T.; Burnham, D. R.; Smith, P. B.; Chiu, D. T. *Angew. Chem.* **2010**, *122*, 9626–9630.
(15) Schirhagl, R.; Chang, K.; Loretz, M.; Degen, C. L. *Annu. Rev. Phys. Chem.* **2014**, *65*, 83–105.
(16) Widengren, J.; Rigler, R. *Bioimaging* **1996**, *4*, 149–157.
(17) Spikes, J. D. *Photochem. Photobiol.* **1984**, *39*, 797–808.
(18) Nadort, A.; Zhao, J.; Goldys, E. M. *Nanoscale* **2016**, *8*, 13099–13130.
(19) Pàmies, P. *Nat. Mater.* **2015**, *14*, 966.
(20) Shang, L.; Nienhaus, K.; Nienhaus, G. U. *J. Nanobiotechnology* **2014**, *12*, 5.
(21) Moore, T. L.; Rodriguez-Lorenzo, L.; Hirsch, V.; Balog, S.; Urban, D.; Jud, C.; Rothen-Rutishauser, B.; Lattuada, M.; Petri-Fink, A. *Chem. Soc. Rev.* **2015**, *44*, 6287–6305.
(22) Haziza, S.; Mohan, N.; Loe-Mie, Y.; Lepagnol-Bestel, A.-M.; Massou, S.; Adam, M.-P.; Le, X. L.; Viard, J.; Plancon, C.; Daudin, R. *Nat. Nanotechnol.* **2017**, *12*, 322.
(23) Hoshyar, N.; Gray, S.; Han, H.; Bao, G. *Nanomedicine* **2016**, *11*, 673–692.
(24) Choi, H. S.; Liu, W.; Misra, P.; Tanaka, E.; Zimmer, J. P.; Ipe, B. I.; Bawendi, M. G.; Frangioni, J. V. *Nat. Biotechnol.* **2007**, *25*, 1165–1170.
(25) Ernsting, M. J.; Murakami, M.; Roy, A.; Li, S.-D. *J. Control. Release* **2013**, *172*, 782–794.
(26) Moghimi, S. M.; Hunter, A.; Andresen, T. *Annu. Rev. Pharmacool. Toxicol.* **2012**, *52*, 481–503.
(27) Montalti, M.; Cantelli, A.; Battistelli, G. *Chem. Soc. Rev.* **2015**, *44*, 4853–4921.
(28) Fang, C. Y.; Vaijayanthimala, V.; Cheng, C. A.; Yeh, S. H.; Chang, C. F.; Li, C. L.; Chang, H. C. *Small* **2011**, *7*, 3363–3370.
(29) Mohan, N.; Chen, C.-S.; Hsieh, H.-H.; Wu, Y.-C.; Chang, H.-C. *Nano Lett.* **2010**, *10*, 3692–3699.
(30) Harmsen, S.; Teraphongphom, N.; Tweedle, M. F.; Basilion, J. P.; Rosenthal, E. L. *Mol. Imaging Biol.* **2017**, *19*, 357–362.
(31) Haque, A.; Faizi, M. S. H.; Rather, J. A.; Khan, M. S. *Biorg. Med. Chem.* **2017**, *25*, 2017–2034.
(32) Vaijayanthimala, V.; Cheng, P.-Y.; Yeh, S.-H.; Liu, K.-K.; Hsiao, C.-H.; Chao, J.-I.; Chang, H.-C. *Biomaterials* **2012**, *33*, 7794–7802.
(33) Tajiri, K.; Kishi, H.; Ozawa, T.; Sugiyama, T.; Muraguchi, A. *Cytometry Part A* **2009**, *75*, 282–288.
(34) Camejo-Arroyo, S.; Adam, M.-P.; Besbes, M.; Hugonin, J. P.; Jacques, V.; Greffet, J. J.; Roch, J. F.; Hell, S. W.; Treussart, F. *ACS Nano* **2013**, *7*, 10912–10919.
(35) Harke, B.; Keller, J.; Ullal, C. K.; Westphal, V.; Schönle, A.; Hell, S. W. *Opt. Express* **2008**, *16*, 4154–4162.
(36) Tzeng, Y. K.; Faklaris, O.; Chang, B. M.; Kuo, Y.; Hsu, J. H.; Chang, H. C. *Angew. Chem. Int. Ed.* **2011**, *50*, 2262–2265.
(37) Rittweger, E.; Han, K. Y.; Irvine, S. E.; Eggeling, C.; Hell, S. W. *Nat. Photonics* **2009**, *3*, 144.
(38) Hsiao, W. W.-W.; Hui, Y. Y.; Tsai, P.-C.; Chang, H.-C. *Acc. Chem. Res.* **2016**, *49*, 400–407.
(39) Yi, J.; Manna, A.; Barr, V. A.; Hong, J.; Neuman, K. C.; Samelson, L. E. *J. Vis. Exp.* **2017**, *124*, e55997.
(40) Yi, J.; Manna, A.; Barr, V. A.; Hong, J.; Neuman, K. C.; Samelson, L. E. *Mol. Biol. Cell* **2016**, *27*, 3591–3600.
(41) Xu, C.; Zipfel, W.; Shear, J. B.; Williams, R. M.; Webb, W. W. *Proc. Natl. Acad. Sci. USA* **1996**, *93*, 10763–10768.
(42) Schießl, I. M.; Castrop, H. *Pflüg. Arch. Eur. J. Phy.* **2016**, *468*, 1505–1516.
(43) Patterson, G. H.; Piston, D. W. *Biophys. J.* **2000**, *78*, 2159–2162.
(44) Hopt, A.; Neher, E. *Biophys. J.* **2001**, *80*, 2029–2036.
(45) Jimenez, C. M.; Knezevic, N. Z.; Rubio, Y. G.; Szunerits, S.; Boukherroub, R.; Teodorescu, F.; Croissant, J. G.; Hocine, O.; Seric, M.; Raehm, L. *J. Mater. Chem. B* **2016**, *4*, 5803–5808.
(46) Chang, Y.-R.; Lee, H.-Y.; Chen, K.; Chang, C.-C.; Tsai, D.-S.; Fu, C.-C.; Lim, T.-S.; Tzeng, Y.-K.; Fang, C.-Y.; Han, C.-C. *Nat. Nanotechnol.* **2008**, *3*, 284–288.
(47) Hui, Y. Y.; Zhang, B.; Chang, Y.-C.; Chang, C.-C.; Chang, H.-C.; Hsu, J.-H.; Chang, K.; Chang, F.-H. *Opt. Express* **2010**, *18*, 5896–5905.
(48) Wee, T.-L.; Tzeng, Y.-K.; Han, C.-C.; Chang, H.-C.; Fann, W.; Hsu, J.-H.; Chen, K.-M.; Yu, Y.-C. *J. Phys. Chem. A* **2007**, *111*, 9379–9386.
(49) Zhan, Y.; Liu, Y.; Zeng, Q. *J. Vis. Exp.* **2018**, *141*, e58603.
(50) Orth, A.; Ghosh, R. N.; Wilson, E. R.; Doughney, T.; Brown, H.; Reineck, P.; Thompson, J. G.; Gibson, B. C. *Biomed. Opt. Express* **2018**, *9*, 2943–2954.
(51) Taylor, R. M.; Huber, D. L.; Monson, T. C.; Ali, A.-M. S.; Bisoffi, M.; Sillerud, L. O. *J. Nanopart. Res.* **2011**, *13*, 4717–4729.
(52) Prabhakar, N.; Peurla, M.; Koho, S.; Deguchi, T.; Näreoja, T.; Chang, H. C.; Rosenholm, J. M.; Hänninen, P. E. *Small* **2018**, *14*, 1701807.
(53) Scheers, I.; Palermo, J.; Freedman, S.; Wilschanski, M.; Shah, U.; Abu-El-Hajia, M.; Barth, B.; Fishman, D.; Gariepy, C.; Giefer, M., et al. *J Pediatr Gastroenterol Nutr.* **2018**, *67* (2), 232–236.

Fluorescent Silica Nanoparticles

Name	Particle Size (nm)	Emission Max (nm)	Absorption Max (nm)	Cat. No.
Fluorescent silica nanobeads	25	590	570	**797928-5MG**
	50	590	570	**797936-5MG**
	90	590	570	**797898-5MG**
	120	590	570	**797863-5MG**
Ultrastable fluorescent silica nanobeads	25	590	570	**797901-2MG**
	50	590	570	**797952-2MG**
	90	590	570	**797944-2MG**
	120	590	570	**797871-2MG**

Fluorescent Nanodiamonds

Nitrogen Vacancy	Particle Size (nm)	Form	Cat. No.
~ 1.5 ppm NV centers	100	suspension, 1 mg/mL in deionized water	**798142-5ML**
~ 2.5 ppm NV centers	70	suspension, 1 mg/mL in deionized water	**798169-5ML**
~ 3 ppm NV centers	90	suspension, 1 mg/mL in deionized water	**798150-5ML**
	100	suspension, 1 mg/mL in deionized water	**798134-5ML**
≤ 4 NV/particle	35	dispersion, 1 mg/mL in deionized water	**900172-5ML**
> 900 NV/particle	100	powder	**900171-5MG**
> 60 NV/particle	70	dispersion, 1 mg/mL in deionized water	**900173-5ML**
> 900 NV/particle	100	1 mg/mL in deionized water	**900174-5ML**
~ 3 ppm NV centers	140	1 mg/mL in deionized water	**901798-2ML**
	140	powder	**901799-5MG**

Fluorescently Labeled Gold Nanoparticles

Gold Nanorods

Surface Group	Particle Size (nm)	Cat. No.
Cy3 and amine functionalized	10	**905984-1.75MG**
Cy3 and azide functionalized	10	**905909-1.75MG**
Cy3 and maleimide functionalized	10	**905720-1.75MG**
Cy3 and NHS functionalized	10	**905895-1.75MG**
Cy3 and protein A functionalized	10	**905976-1.75MG**
Cy3 and streptavidin functionalized	10	**905968-1.75MG**
FITC and amine functionalized	25	**906174-2.5MG**
FITC and azide functionalized	25	**906220-2.5MG**
FITC and biotin functionalized	25	**906247-2.5MG**
FITC and carboxyl functionalized	25	**906255-500MG**
FITC and maleimide functionalized	25	**906166-2.5MG**
FITC and methyl functionalized	25	**906204-2.5MG**
FITC and NHS functionalized	25	**906239-2.5MG**
FITC and protein A functionalized	25	**906182-2.5MG**
FITC and streptavidin functionalized	25	**906212-2.5MG**

Gold Nanospheres

Surface Group	Particle Size (nm)	Cat. No.
Cy3 and amine functionalized	15	**905623-2.5MG**
Cy3 and azide functionalized	15	**906042-2.5MG**
Cy3 and biotin functionalized	10	**905887-1.75MG**
	15	**905577-2.5MG**
Cy3 and carboxyl functionalized	10	**905852-1.75MG**
	15	**905569-2.5MG**
Cy3 and maleimide functionalized	15	**905631-2.5MG**
Cy3 and methyl functionalized	10	**905712-1.75MG**
	15	**905658-2.5MG**
Cy3 and NHS functionalized	15	**905739-2.5MG**
Cy3 and protein A functionalized	15	**905941-2.5MG**
Cy3 and streptavidin functionalized	15	**905933-2.5MG**
FITC and amine functionalized	100	**905615-2.5MG**

Surface Group	Particle Size (nm)	Cat. No.
FITC and azide functionalized	100	**905593-2.5MG**
FITC and biotin functionalized	100	**905585-2.5MG**
FITC and carboxyl functionalized	100	**905550-2.5MG**
FITC and maleimide functionalized	100	**905666-2.5MG**
FITC and methyl functionalized	100	**905801-2.5MG**
FITC and NHS functionalized	100	**905747-2.5MG**
FITC and protein A functionalized	100	**905836-2.5MG**
FITC and streptavidin functionalized	100	**905755-2.5MG**

Recent Developments in Magnetic Iron Oxide Nanoparticles for Non-Invasive Bioimaging



Yaolin Xu,[1] Y. Andrew Wang,[2] and Hui Mao*[1]

[1]Department of Radiology and Imaging Sciences, Emory University School of Medicine, Atlanta, Georgia 30322, USA
[2]Ocean Nanotech, LLC, 7964 Arjons Drive, San Diego, California 92126, USA
*E-mail: hmao@emory.edu

Introduction

Non-invasive imaging is a valuable tool for the detection and diagnosis of disease, as well as for monitoring patients' response to treatment. With the rapid advances in technology and increased availability and accessibility of imaging equipment and capability, the number of radiological examinations has grown significantly in the past decade — an estimated 280 million clinical imaging tests are performed annually in the US alone.[1,2] Disease-specific and targeted imaging and drug delivery techniques have been actively pursued in recent years for precision medicine, where biomarker targeting, high sensitivity, and high resolution are often required. Imaging contrast agents are often used to enhance both contrast and sensitivity of lesion detection and quantitative measurements of physiological and pathological conditions, thus enabling more accurate diagnoses and proper treatment decisions. Many new nanomaterial-based contrast agents and imaging probes have been introduced, promising to expand the capabilities and applications of non-invasive imaging, as well as image-guided interventions, to advance clinical practice. For example, magnetic resonance imaging (MRI) is one of the most informative diagnostic imaging modalities because it is radiation-free, and offers high spatial resolution, soft tissue contrast, and reveals diverse image features associated with various tissue characteristics. The unique chemical and physical properties of magnetic nanomaterials offer many advantages for non-invasive, biomarker-targeted MRI applications,[3] especially when compared to clinically used, low molecular weight gadolinium (Gd) chelate contrast agents. These FDA approved Gd^{3+}-chelates, e.g., Gd-DTPA (Magnevist®), can amplify the signal or contrast of the tissue under examination based on changes in longitudinal relaxation time, i.e., T_1, because the seven unpaired electrons of paramagnetic Gd^{3+} have high longitudinal relaxivity ($r_1 \approx 4–8$ $mM^{-1}{\cdot}s^{-1}$), which can be further increased by properly selecting the chelate ligands.

On the other hand, superparamagnetic iron oxide nanoparticles (SPIO or IONPs) typically provide a different contrast-enhancing mechanism. They shorten the transverse relaxation time, i.e., T_2 and T_2*, by generating imaging contrast that mainly suppresses the signal from affected tissue or organs. While clinical uses of magnetic IONP-based contrast agents, e.g., Feridex®, have declined significantly in recent years due to their limited applicability, IONPs have been widely used to develop platforms for targeted molecular imaging and theranostic applications that take advantage of the unique properties of magnetic nanomaterials. In addition to their excellent biocompatibility, IONPs have 1) strong and tunable magnetic properties, which result in superb contrast-enhancing effects, 2) favorable pharmacokinetic properties with prolonged blood and tissue retention times, and 3) diverse surface chemistry, which allows functionalization of IONPs for multimodal imaging, biomarker targeting, and delivery of therapeutics as illustrated in **Figure 1**. With recent advances in molecular imaging and the increasing need for precise, functional imaging for both diagnosis and therapy, there is renewed interest in developing new IONPs for use in biomedical imaging.

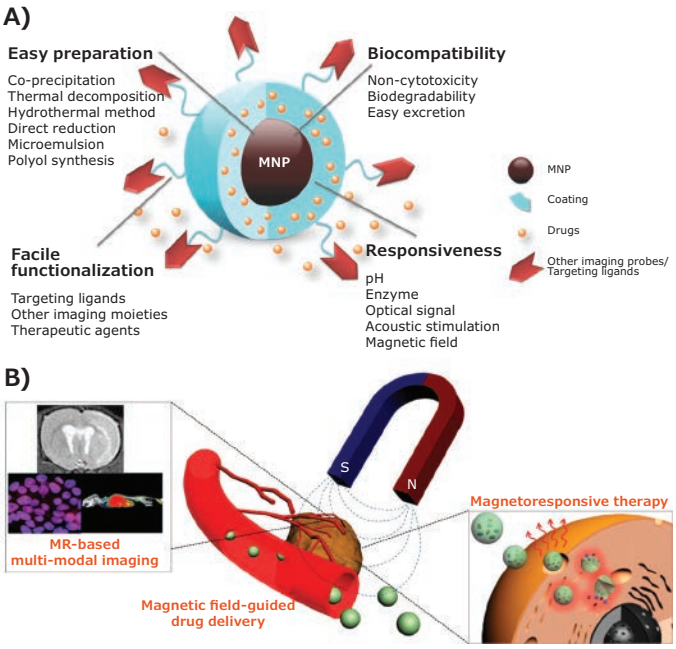

Figure 1. Magnetic nanoparticles (MNP): **A**) Advantages and properties for developing imaging applications, and **B**) some examples of biomedical applications. Adapted with permission from references 5 and 7 copyright 2016 Wiley-VCH and copyright 2015 ACS respectively.

Since many excellent reviews have recently been published describing the chemistry, properties, and imaging applications of MNP, including ours,[4,5] this article will focus on three areas of magnetic IONPs: 1) shape control and renal-clearable sub-5 nm IONPs with T_1 or dual T_1-T_2 MRI contrast enhancing capabilities, 2) magnetic particle imaging (MPI) applications that solely depends on specific IONPs, 3) multifunctional IONPs for use in hybrid MRI (MRI combined with optical and/or nuclear imaging).

Sub-5 nm IONPs as T_1 or T_1-T_2 Dual MRI Contrast Agents

While IONP-based agents are highly biocompatible, and are in fact used for clinically treating iron deficiency, there are increasing concerns about poor clearance and long liver retention time for the large IONPs (i.e., 10–50 nm core) currently used in biomedical imaging applications. Moreover, increasing incidents of severe nephrogenic systemic fibrosis (NSF) caused by free Gd^{3+} ions leaching out of their complex, limit the clinical applications of Gd-based T_1 contrast agents from patients with renal dysfunctions. This has accelerated efforts to develop IONPs with both excellent T_1 contrast and a better clearance profile.

Traditionally, IONPs are used as T_2 "darkening" contrast agents, because nearby magnetic IONPs affect the T_2 relaxation time of the hydrogen atoms in water molecules, a main source of the signal for MRI. Transverse relaxivity (r_2) correlates directly with the IONP size. As IONP size increases from 4 to 6, 9, and 12 nm, r_2 values gradually rise from 78 to 106, 130, and 218 $mM^{-1}{\cdot}s^{-1}$ (at a field strength of 1.5 T). The high r_2 values and r_2/r_1 ratios (ca. 10) of conventional IONPs, with core size ranges from 10–50 nm, make IONPs excellent T_2 contrast "darkening" agents, but not the clinically preferred T_1 "brightening" contrast agents.[5] In order to "tune" the relaxivities for gaining T_1 contrast, low dimensional IONPs were developed, including ultrathin iron oxide nanowhiskers with diameters of less than 3 nm and ultra-fine iron oxide nanoparticles (uIONPs) were developed.[6,7] Shown in **Figure 2A–C**, ultrathin iron oxide nanowhiskers that were 20 nm long and 2 nm in diameter with r_1 of 6.13 $mM^{-1}{\cdot}s^{-1}$ and r_2/r_1 ratio of 1.83 enhanced the T_1 contrast in T_1 weighted spin echo images of both phantoms and rats received subcutaneous and intraperitoneal injection of nanowhiskers.

Sub-5 nm uIONPs also show promise as T_1 weighted contrast agents, due to their biocompatibility and their Gd^{3+}-comparable r_1 value (4–5 $mM^{-1}{\cdot}s^{-1}$) and low r_2/r_1 ratio (<4) resulting from the ultra-small size (below 5 nm) and high surface-to-volume ratio.[6,8] With an r_1 comparable to Gd-DTPA, uIONPs exhibit excellent T_1 contrast for vascular imaging after intravenous administration of uIONPs in mice, and can help delineate blood vessels and enhance tumor images (**Figure 2E**).[6] Moreover, a novel dual T_1–T_2 contrast effect was observed in mice, where T_1 brightening contrast was observed in the hepatic vasculature while T_2 (or darkening) contrast presented in the liver parenchyma (**Figure 2F**). This dual T_1–T_2 contrast effect not only opens potential clinical applications for simultaneous imaging of the vasculature and liver parenchyma, but also enables revealing tissue characteristics and locations where uIONPs accumulated. More importantly, uIONPs can be secreted through the kidney after imaging studies, improving the biocompatibility and clearance and thus the safety profile of the imaging agent. A recent study using uIONPs as imaging probes revealed that nanoparticles with sub-5 nm sizes also exhibit the enhanced permeability and retention (EPR) effect,[7] one of the main driving forces for delivery of nanoparticles to tumors, and therefore improve delivery to tumors and subsequent intratumoral distribution. In this case, the bright to dark T_1–T_2 contrast switch caused by changing the form of uIONP dispersion in different tissue environments confirmed the delivery and tissue penetration of uIONPs, based on the appearance of bright T_1 contrast followed by the uIONP clustering in the tumor after accumulation. Quantitative histological analysis confirmed that sub-5 nm nanoparticles can be delivered to the tumors much more effectively than their larger IONP counterparts.

IONPs as Magnetic Particle Imaging (MPI) Contrast Agents

Magnetic particle imaging (MPI) is an emerging, non-invasive, tomographic imaging technique that has been recently been used as a preclinical imaging tool. The MPI signal is derived from the nonlinear magnetization behaviors of IONPs with an applied magnetic field. When IONPs are present in tissue in an external magnetic field, the magnetization of IONPs can be manipulated by applying the electromagnetic energy. Because of the nonlinear magnetization behavior of IONPs,

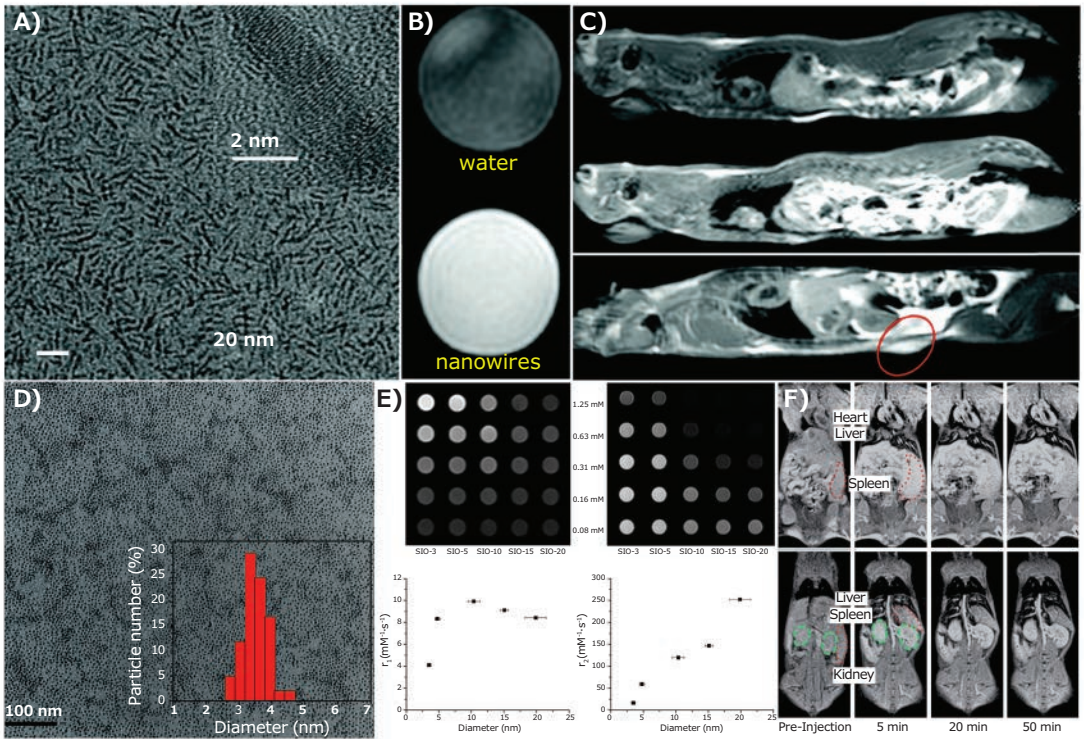

Figure 2. A) Transmission electron microscopy (TEM) image, and T_1-weighted spin echo images of **B**) phantom and **C**) rat after intraperitoneal (**middle**) or subcutaneous (**bottom**) injection of iron oxide nanowhiskers, as compared to control rat (**top**), adapted with permission from reference 8, copyright 2018 Royal Society of Chemistry; **D**) TEM image of uIONPs; **E**) T_1-, T_2-weighted spin echo images, r_1 and r_2 values of different sized IONPs; **F**) Fat-suppressed T_1-weighted spin echo images of a mice before and after administration of uIONPs at 10 mg·kg^{-1}. Spleen highlighted in red dotted circles, and kidney in green dashed circles. Adapted with permission from reference 6, copyright 2014 Royal Society of Chemistry.

higher harmonics of the excitation frequency can be detected at the IONPs. Intensity of harmonic reflects the presence and characteristics of IONPs.[11] Given that MPI signals exclusively rise from IONPs, this imaging method shows high sensitivity with little or no background, therefore offering high contrast or "hot spot" images and accurate quantification of the imaging agent. This is similar to nuclear imaging, but without the disadvantages involved in radioisotopic labels. When compared to MRI systems at typical field strengths (1.5–7 T), MPI has superb sensitivity (near pictogram of Fe) with high image acquisition rates (up to 40 volumes/second). Because the MPI signal intensity is proportional to the concentration of IONPs, it allows quantitation of IONPs at the region of interest without interference from a background signal.

Among all possible design specifications for IONPs (core size, hydrodynamic size, surface chemistry, composition, biocompatibility, blood circulation time, etc.), IONP size and uniformity are the major factors in determining MPI signal strength and spatial resolution.[9,10] Early work indicated that, at each operating frequency, there was an optimal core size for specific sizes of IONPs. For example, IONP with a core size of 20 nm yields optimal MPI images at 25 kHz, while 15 nm IONPs provide optimal images at 50 kHz.[11] Further investigations are needed to fully understand the relationship between IONP characteristics and signal and spatial resolution. It should be noted that MRI or CT images are needed to provide anatomic information for MPI, since it only provides "hot-spots," from where IONPs are present and does not show the structure and morphological details of tissue or organs of interest.

The first *in vivo* application of MPI with Ferucarbotran (Resovist®, an IONP-based MRI contrast agent with a mean hydrodynamic diameter of 60 nm) was able to show the left and right atrium, ventricle, and the pulmonary veins of the heart structure in a mouse (**Figure 3A**). Cell tracking and targeted imaging are two of the earliest applications of MPI. For example, neural progenitor cells labeled with Resovist® were imaged and quantified *in vivo* in an immunosuppressed rat model over more than 80 days. The detection limit for cell tracking studies was determined to be ~100 cells for Resovist®-labeled stem cells with current MPI systems.[10] In an investigation of red blood cells (RBC) migration, significant MPI signals were generated from SPION (Resovist® and Sinerem® (diameter of 20–40 nm))-labeled RBC in the high frequency range, when compared to control RBC without SPION labeling (**Figure 3B–C**). Interestingly, the SPION-labeled RBC exhibited a long blood half-life, demonstrating the possibility of using MPI for real-time monitoring the blockage and impediments in circulatory systems.

MPI can be also used to visualize and track interventional medical devices and implants. In **Figure 3D–E**, a balloon catheter, commercially available for percutaneous intraluminal angioplasty, was filled with Resovist® tracers and inserted within

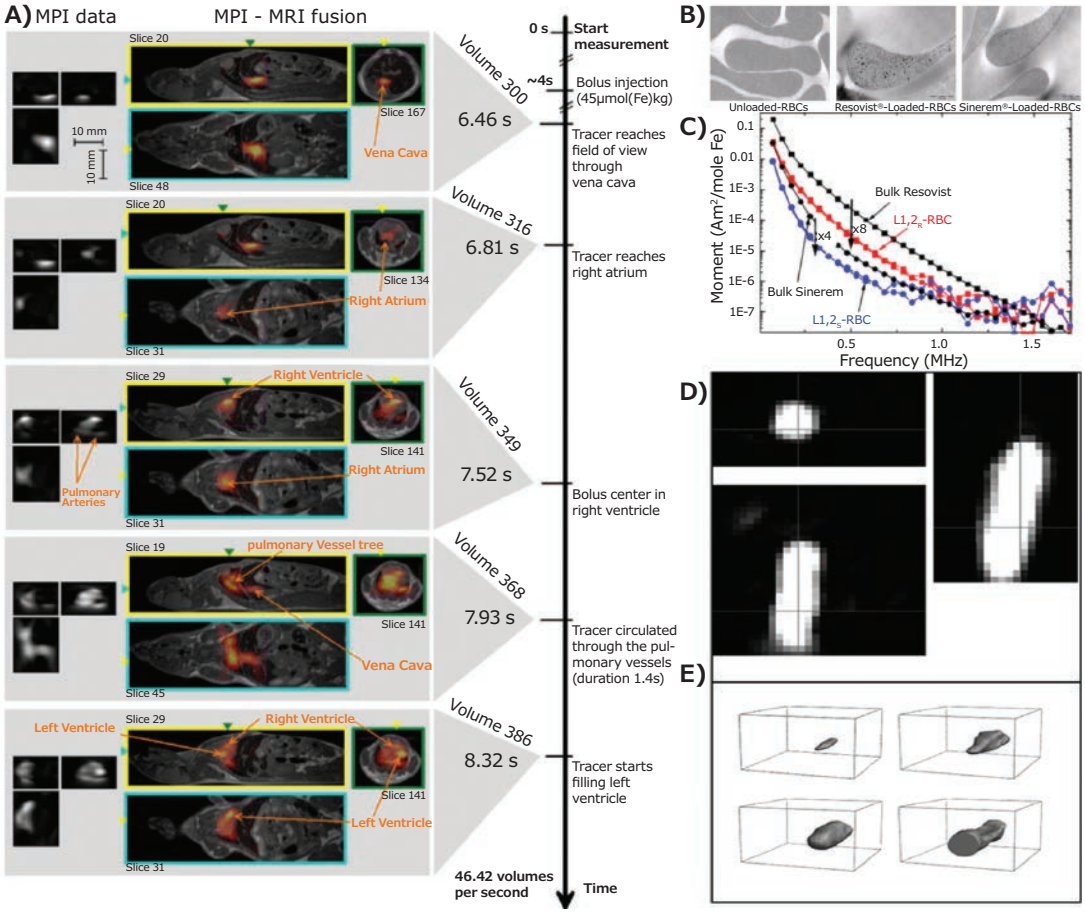

Figure 3. A) Dynamic images of MPI (**left**) and MPI-MRI fusion (**right**) of a beating mouse heart; B) TEM images of control and NP-labeled red blood cells and C) MPI signal data for Resovist®, Sinerem®, Resovist®-labeled and Sinerem®-loaded red blood cells ($L_{1,2R}$-RBC and $L_{1,2S}$-RBC, respectively); D) the MPI axial, coronal, and sagittal-view of balloon catheter filled with IONPs (Resovist®), and E) 3D rendering images of balloon being deflated (**top left**), during inflation (**top right**), inflated (**bottom left**), and being moved out of the field of view (**bottom right**). Adapted with permission from reference 12, copyright 2013 Royal Society of Chemistry.

a vascular phantom, and then imaged with a MPI scanner.[12] With only a small amount of MPI tracer (25 mmol of iron per liter), the shaft was clearly visible with MPI, as were the balloon inflation and deflation processes, and the arterial stenosis dilation.

IONP-based Multimodal Imaging

Given the respective strengths and limitations of specific imaging modalities associated with the sensitivity, resolution, anatomic information, and cost, there has been a growing interest in developing multimodal imaging systems, that can combine and complement two different imaging modalities.

MRI-near Infrared (NIR) Optical Imaging

Coupling the three-dimensional, anatomically-defined deep tissue imaging capability of MRI with cost effective optical imaging and functional molecular imaging probes can provide more information about specific biological and molecular events *in vivo*. Furthermore, optical imaging-based surgical interventions can take advantage of the high spatial resolution and anatomic information from MRI. Among the various optical imaging probes, NIR dyes have advantages over conventional fluorescent fluorophores because of the minimal absorption interference and autofluorescence from biological samples, reduced scattering issues, and improved tissue penetration depth.

To combine NIR optical imaging with MRI, NIR dyes can be conjugated to IONPs. For example, Cy5.5 is a widely available NIR dye. It was conjugated to dextran-coated, crosslinked IONPs through amine-reactive crosslinkers, and then further modified with synthetic peptides (EPPT) as a targeting ligand to image underglycosylated mucin-1 (uMUC-1) antigens on human pancreatic adenocarcinoma. Twenty-four hours after intravenous administration of the targeting probes, a significant T_2 contrast was observed within tumor areas (**Figure 4A**) accompanied with a high-intensity NIR fluorescence signal (**Figure 4B**).[7] Similarly, a Cy5.5-labeled urokinase-type plasminogen activator receptor (uPAR)-targeting IONP probe was prepared to image breast tumors in mice. After conjugating the Cy5.5 and amino-terminal fragment (ATF) peptides onto IONPs, both MRI and NIR imaging were used to visualize the uPAR expressed tumors (circled in **Figure 4C** and **4D**).[4] Similarly, the use of tumor-targeting, insulin-like growth factor 1 (IGF-1) and NIR830 dye onto IONPs

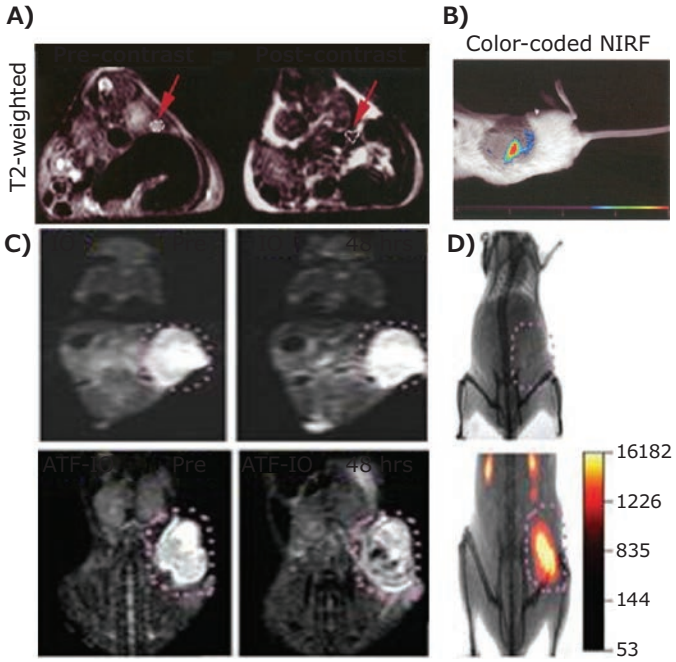

Figure 4. A) T_2-weighted images and B) color-coded NIR mapping of Cy5.5-EPPT-CLIO-injected mice bearing human pancreatic adenocarcinoma, adapted with permission from reference 7, copyright 2015 American Chemical Society; C) T_2-weighted MRI and D) NIR imaging of Cy5.5-ATF-IONP-injected mice bearing 4T1 mouse mammary tumors. Adapted with permission from reference 4, copyright 2012 Ivyspring International.

demonstrated the targeted MRI-NIR imaging abilities of the IGF-1 receptor positive pancreatic tumor model.[5] Besides added imaging capability and information by adding a complementary modality, the NIR dye conjugated IONP, including commercially available ones (MagDye-765®, IN765-05-05) impart favorable pharmacokinetics and biomarker targeting, that are not available with low molecular weight optical imaging probes. However, the interference of IONPs with the optical properties of the original dyes, e.g., optical quenching effect, needs to be considered when combining two materials.

MRI-Positron Emission Tomography (PET)

PET is the most powerful clinical molecular imaging modality. It is capable of reporting functional, molecular, and metabolic information about diseases using radioactive, positron-emitting tracers. Combined PET-MRI scanners, which use MRI to visualize anatomic structures and tissue morphology, can reveal functional, molecular, and physiological information to enhance diagnosis. The combined PET-MRI is now available for clinical use. It is anticipated that as combined PET-MRI are used in more and different ways, the need for novel contrast materials that enhance both MRI and PET detection will increase. Traditional MRI-PET dual contrast agents were prepared by integrating a compound labeled with PET sensitive radioisotopes (e.g., ^{18}F, ^{64}Cu, ^{69}Ge) with IONPs through chelating ligands, such as 1,4,7,10-tetraazacyclododecane-1,4,7,10-tetraacetic acid (DOTA, **Cat. No. 86734**) or 1,4,7-triazacyclononane-N,N′,N″-triacetic acid (NOTA). ^{64}Cu-bis(dithiocarbamatebisphosphonate) [^{64}Cu-$(dtcbp)_2$], which coupled IONPs with the PET isotope ^{64}Cu (shown in **Figure 5A**) was developed to track ^{64}Cu labeled IONPs in draining lymph nodes of mice by dual-imaging systems (**Figure 5B**).[13] Recent advances in radiochemistry allow the synthesis of hybrid MRI-PET tracers without the need for chelators. **Figure 5C** shows germanium (^{69}Ge with $t_{1/2}$ of 39.05 h) can be doped into IONPs during chemical synthesis by mixing ^{69}Ge with iron precursors. This material showed excellent contrast in T_2 weighted MRI and ^{69}Ge PET.[7] To obtain T_1 MRI contrast agents with PET imaging capability, ^{68}Ga was doped into dextran-coated uIONPs using a microwave assisted route (**Figure 5D**), resulting in brighter T_1 weighted MRI images and PET images from ^{68}Ga-uIONPs at several iron concentrations (**Figure 5E**).[6,14]

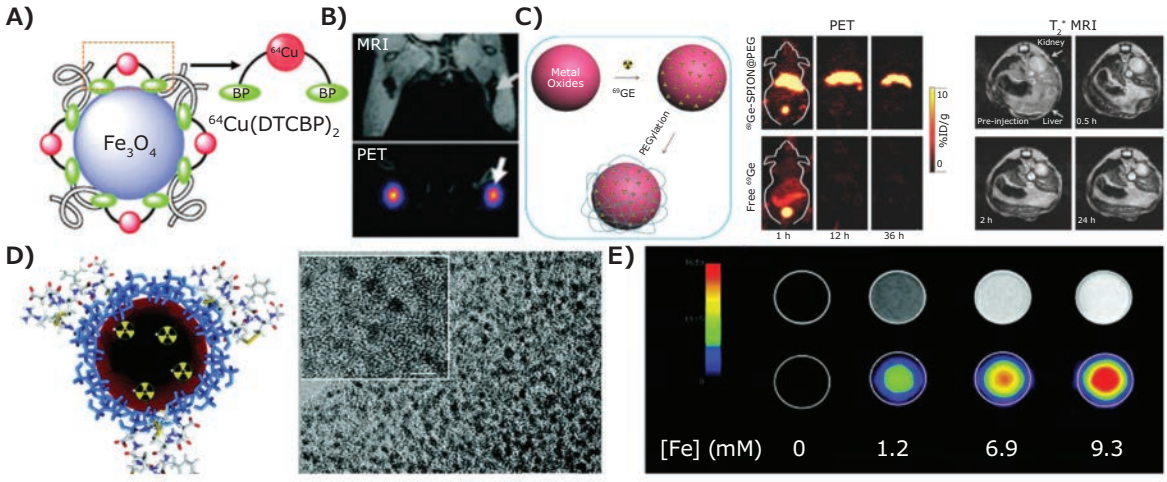

Figure 5. A) Schematic drawing of IONP-^{64}Cu chelate; B) MRI/PET dual-mode imaging of lymph nodes with ^{64}Cu-$(dtcbp)_2$-IONPs, adapted with permission from reference 13, copyright 2018 Elsevier; C) schematic drawing of ^{69}Ge-doped IONPs, and *in vivo* PET and T_2-weighted MRI images, adapted from reference 7, copyright 2015 American Chemical Society; D) schematic drawing and TEM image of ^{68}Ga-uIONPs, and E) MRI phantom images (**top**) and PET scan (**bottom**) of ^{68}Ga-uIONPs at different iron concentrations. Adapted with permission from reference 8, copyright 2018 Royal Society of Chemistry.

Conclusions

Magnetic IONPs will remain a major platform of choice for development and application of bioimaging, for both preclinical and translational research, as well as potentially for clinical imaging. We have highlighted recent developments in the design and engineering of IONPs as contrast agents for MRI-, MPI-, and MRI-centric multimodal imaging. The growing interest in IONPs as alternatives to Gd-DTPA as a T_1 MRI contrast agent will lead to further development of this new class of IONPs for clinical use. With several multi-modal imaging modalities already available for clinical applications, formulating multifunctional, hybrid IONP agents that combine contrast-enhancing effects in multiple imaging modalities will continue to be an active area of research and development. Although it may be years before MPI is developed and approved for clinical applications, its rapid adaptation in preclinical research will be sufficient to demonstrate its capabilities and potential to expand the use of *in vivo* bioimaging. In the case of MPI, which requires magnetic IONPs, the development of new classes of IONPs tuned or tailored for MPI applications will be an exciting area to watch.

References

(1) Nanotechnology for Biomedical Imaging and Diagnostics: From Nanoparticle Design to Clinical Applications. John Wiley & Sons, Inc.: Hoboken, New Jersey, **2015**.
(2) http://www.mach7t.com/resources/infographics/annual-diagnostic-imaging-tests-infographic/.
(3) Kim, D.; Kim, J.; Park, Y. I.; Lee, N.; Hyeon, T., *ACS Cent. Sci.* **2018**, *4* (3), 324–336.
(4) Huang, J.; Zhong, X. D.; Wang, L. Y.; Yang, L. L.; Mao, H. *Theranostics* **2012**, *2* (1), 86–102.
(5) Huang, J.; Li, Y. C.; Orza, A.; Lu, Q.; Guo, P.; Wang, L. Y.; Yang, L.; Mao, H. *Adv. Funct. Mater.* **2016**, *26* (22), 3818–3836.
(6) Huang, J.; Wang, L. Y.; Zhong, X. D.; Li, Y. C.; Yang, L. L.; Mao, H. *J. Mater. Chem. B* **2014**, *2* (33), 5344–5351.
(7) Lee, N.; Yoo, D.; Ling, D.; Cho, M. H.; Hyeon, T.; Cheon, J. *Chem. Rev.* **2015**, *115* (19), 10637–10689.
(8) Bao, Y.; Sherwood, J. A.; Sun, Z. *J. Mater. Chem. C* **2018**, *6* (6), 1280–1290.
(9) Knopp, T.; Gdaniec, N.; Moddel, M. *Phys. Med. Biol.* **2017**, *62* (14), R124–R178.
(10) Panagiotopoulos, N.; Duschka, R. L.; Ahlborg, M.; Bringout, G.; Debbeler, C.; Graeser, M.; Kaethner, C.; Ludtke-Buzug, K.; Medimagh, H.; Stelzner, J.; Buzug, T. M.; Barkhausen, J.; Vogt, F. M.; Haegele, J. *Int. J. Nanomed.* **2015**, *10*, 3097–3114.
(11) Bauer, L. M.; Situ, S. F.; Griswold, M. A.; Samia, A. C. S. *J. Phys. Chem. Lett.* **2015**, *6* (13), 2509–2517.
(12) Pablico-Lansigan, M. H.; Situ, S. F.; Samia, A. C. S. *Nanoscale* **2013**, *5* (10), 4040–4055.
(13) Polo, E.; del Pino, P.; Pardo, A.; Taboada, P.; Pelaz, B. (**2018**) In: Gonçalves, G.; Tobias, G. (eds) *Nanooncology, Springer*.
(14) Fernandez-Barahona, I.; Munoz-Hernando, M.; Pellico, J.; Ruiz-Cabello, J.; Herranz, F. *Appl. Sci. (Basel)* **2018**, *8* (7), 1–26.

Iron Oxide Nanoparticles

Functional Group	Form	Composition	Particle Size (nm)	Cat. No.
amine	dispersion	1 mg/mL in H_2O	15	**900199-10ML**
	dispersion	1 mg/mL in H_2O	25	**900028-10ML**
biotin	dispersion	1 mg/mL (in 10 mM PBS buffer)	15	**900037-1ML**
carboxylic acid	dispersion	5 mg/mL in H_2O	15	**900200-2ML**
	dispersion	5 mg/mL in H_2O	25	**900201-2ML**
dextran	dispersion	10 mg/mL in H_2O	5	**900147-2ML**
NHS ester	powder		25	**900034-1G**
	powder		15	**900041-1G**
oleic acid	dispersion	5 mg/mL in chloroform	5	**900082-5ML**
	dispersion	5 mg/mL in toluene	15	**900063-5ML**
	dispersion	5 mg/mL in toluene	25	**900064-5ML**
	dispersion	5 mg/mL in toluene	30	**900081-5ML**
	dispersion	5 mg/mL in chloroform	15	**900083-5ML**
	dispersion	5 mg/mL in chloroform	20	**900088-5ML**
	dispersion	5 mg/mL in chloroform	25	**900089-5ML**
	dispersion	5 mg/mL in chloroform	30	**900090-5ML**
PEG	dispersion	1 mg/mL in H_2O	15	**900026-10ML**
	dispersion	1 mg/mL in H_2O	25	**900027-10ML**
rhodamine B	dispersion	1 mg/mL in H_2O	10	**900146-2ML**

Functional Group	Form	Composition	Particle Size (nm)	Cat. No.
streptavidin	dispersion	1 mg/mL in H_2O	10	**900091-1ML**
--	dispersion	1 mg/mL in H_2O	15	**900092-1ML**
	dispersion	1 mg/mL in H_2O	20	**900093-1ML**
	dispersion	1 mg/mL in H_2O	25	**900094-1ML**
	dispersion	1 mg/mL in H_2O	30	**900148-1ML**
	dispersion	20 wt. % in water	<5	**796093-100ML**
	dispersion	5 mg/mL in H_2O	10	**725358-5ML**
	dispersion	5 mg/mL in H_2O	15	**900043-5ML**
	dispersion	5 mg/mL in H_2O	20	**725366-5ML**
	dispersion	5 mg/mL in H_2O	25	**900042-5ML**
	dispersion	5 mg/mL in H_2O	30	**900062-5ML**
	dispersion	5 mg/mL in chloroform	10	**900084-5ML**
	dispersion	5 mg/mL in H_2O	3	**725331-5ML**
	nanoparticles	15 wt. % in ethanol	≤110	**720712-100G**
	nanoparticles	20 wt. % in H_2O	≤110	**720704-100G**
	nanopowder		<50	**544884-5G** **544884-25G**
	solution	5 mg/mL in toluene	10	**700312-5ML**
	solution	5 mg/mL in toluene	20	**700304-5ML**
	solution	5 mg/mL in toluene	5	**700320-5ML**

Increasing the Sensitivity of Lateral Flow Diagnostic Assays with Ultra-Bright Gold Nanoshell Reporters

Steven J. Oldenburg

nanoComposix, San Diego, CA 92111, USA
E-mail: steve.oldenburg@nanocomposix.com

Introduction

Lateral flow assays (also known as immunochromatographic assays) detect or quantify biomolecules in complex samples including blood, urine, saliva, or other fluids to diagnose a variety of medical conditions.[1] They are usually self-contained, portable devices that are easy to use, fast, and inexpensive. Lateral flow test devices can be stored at ambient temperature, have a long shelf life, and provide diagnostic results without complex sample processing or additional equipment, making them ideal for both point-of-care and field-based diagnostic uses. Hundreds of millions of lateral flow tests are used each year for a wide variety of applications, including the ubiquitous pregnancy test (**Figure 1**). The sensitivity of these assays depends on the components used, how the components and sample are treated, and the properties of the nanoscale reporter particles that generate the diagnostic signal. The reporter particles are labeled with a molecule — often an antibody or nucleic acid — that recognizes the analyte in the sample and binds to a specific physical location on the strip. To maximize the sensitivity of the assay, reporters are chosen to be as "bright" as possible, generating the largest possible signal intensity per binding event. The reporter particle must also be very small, typically on the nanoscale, so that it can effectively bind to molecular targets.

Lateral flow assays consist of a series of inexpensive, paper-like components that are assembled onto a backing card for handling (**Figure 2**). Components of lateral flow strips typically include:

- Sample pad: Absorbs sample and controls distribution and flow of sample onto the conjugate pad

Figure 1. Image of commonly used lateral flow rapid test for determining pregnancy.

- Conjugate pad: Dispenses and dries nanoparticle-antibody conjugates, ensuring controlled release of conjugate onto the nitrocellulose membrane upon hydration
- Nitrocellulose membrane: Immobilizes the Test line and Control line reagents
- Wicking pad: Provides uniform capillary flow through the membrane, absorbs applied sample, and prevents backflow

Each component overlaps the previous one by at least 1 mm, which allows the sample to flow unimpeded from the sample pad all the way to the wicking pad.

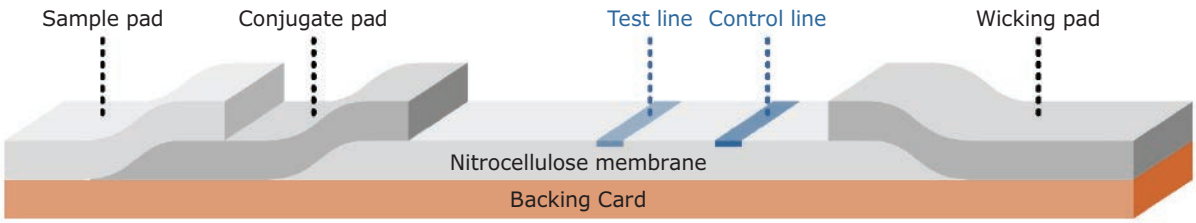

Figure 2. Schematic of lateral flow test strip.

To use a lateral flow rapid test, a liquid sample such as blood, serum, plasma, urine, saliva, or solubilized solids is placed on the sample pad; capillary action then draws the sample through the lateral flow device. The sample pad is sometimes treated with reagents to adjust the pH of the sample, or can contain filters to remove unwanted particulates such as red blood cells. The sample flows from the sample pad to the conjugate pad, which contains dried, strongly colored or fluorescent nanoparticles with antibodies conjugated to their surface. When the sample reaches the conjugate pad, the nanoparticles are rehydrated and mixed with the sample. The mixture then flows through the nitrocellulose membrane and across one or more test lines and a control line. The test and control lines are comprised of immobilized proteins that interact with the sample and generate a signal. The strength of the signal corresponds to the amount of analyte or conjugate present. The remaining fluid is absorbed by a wicking pad that is designed to capture the sample and prevent backflow. Once all the sample has finished running, the signal contrast at the test line(s) can be read by either visual interpretation or using a reader to identify the presence of the analyte, and thus the results.

Lateral Flow Assay Formats

The two most common lateral flow assay formats are "sandwich" and "competition" (**Figure 3**). The sandwich assay format is typically used for detecting larger analytes that have at least two epitopes (binding sites). In most cases, an antibody to one epitope is conjugated to the nanoparticle (the detection antibody on the reporter particle), and an antibody to another epitope is used for the assay's test line (capture antibody). If there is analyte in the sample, it binds to both the detection and capture antibodies, creating a sandwich between the nanoparticle conjugate and the test line to produce a positive signal. If no analyte is present, the nanoparticle conjugate doesn't bind to the capture antibody and no signal is observed. Sandwich assays result in a signal intensity on the test line that is directly proportional to the amount of analyte present in the sample.

The competition assay format is used to detect analytes when antibody pairs are unavailable, or if the analyte is too small for multiple antibody binding events, such as steroids or small organic molecule drugs. In this format, the test line typically contains the analyte molecule, usually a protein-analyte complex. If the target analyte is present in the sample, it binds to the reporter particle and prevents it from binding to the analyte embedded in the test line. If no analyte is present, the reporter particles bind to the analyte embedded in the test line, yielding a signal. In the competition format, signal intensity is inversely proportional to the amount of analyte present in the sample.

In both assay formats, an anti-species antibody is used as the control line, binding the conjugated antibody regardless of test line result. Presence of a control line confirms proper flow and functionality of the assay.

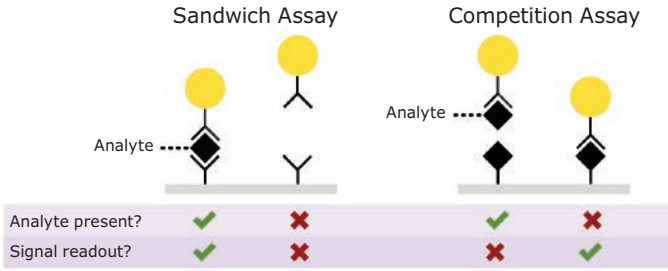

Figure 3. Depiction of "Sandwich" and "Competition" assay formats. In a sandwich assay, a positive signal indicates the presence of analyte and the test line intensity is proportional to the amount of analyte available in the sample. For a competition assay, a strong signal on the test line means little or no analyte is present. This signal intensity is inversely proportional to the analyte concentration.

Nanoparticles as Reporters in Lateral Flow

Lateral flow tests generate an optical signal from strongly colored or fluorescent particles that are bound to test lines on a white nitrocellulose strip. This signal can be read by eye (qualitative or semi-quantitative) or by an optical reader (quantitative). To maximize the sensitivity of the test, each binding event between an analyte and reporter particle should produce the strongest signal possible. While larger particles typically provide a stronger signal per binding event, particles that are too large don't easily flow through the nitrocellulose membrane and have limited opportunity to bind to the test line. Thus, particles that are between 20 nm and 500 nm in diameter are typically selected for use in lateral flow assays. Fluorescent particles can also be employed, and the same general rules apply: the more potent the fluorescence per binding event, the stronger the signal.

One of the most common reporter particles used in diagnostic assays are gold nanoparticles, often referred to as gold colloid.[2] Gold nanoparticles have unusual optical properties that make them exceptionally strong absorbers of light. For example, 40 nm diameter gold nanospheres strongly absorb light at wavelengths near 520 nm, resulting in a ruby red test line.

The gold surface has a natural affinity for antibodies and other proteins, allowing fabrication of nanoparticle-antibody conjugates by simply mixing gold nanoparticles with an affinity ligand. Other sizes and shapes of gold nanoparticles have also been used as lateral flow probes. Gold nanoshells with a 150 nm diameter provide a higher contrast per binding event — typically providing a 5–20 fold increase in sensitivity as compared to 40 nm gold nanospheres. Gold nanoshells are prepared by the electroless deposition of metallic gold onto the surface of a silica particle that is studded with small gold nanoparticles.[3] The small gold seeds grow progressively larger, until they coalesce into a complete shell. (**Figure 4**)

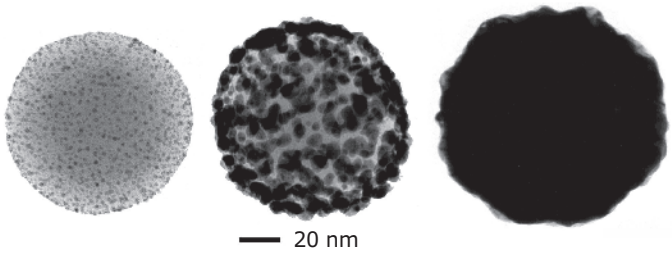

Figure 4. Transmission electron microscopy images of different stages of nanoshell growth. Initially, thousands of ~2 nm gold nanoparticle seeds are bound to positively charged silica nanospheres (**left**). Gold ions in solution are electrolessly deposited onto the bound gold seed, growing the seeds larger (**middle**) until they coalesce into a complete shell (**right**).

By controlling the size of the silica core and the thickness of the gold shell during gold nanoshell synthesis, the peak wavelength of the nanoshells can be tuned to change the particle's color. To maximize sensitivity in lateral flow assays, blue-gray 150 nm gold nanoshells with a 120 nm diameter silica core and a ~15 nm gold shell have been developed. The silica core has a much lower mass than gold, improving the settling time and flow characteristics in the nitrocellulose membrane relative to solid gold particles. **Figure 5** compares the optical extinction

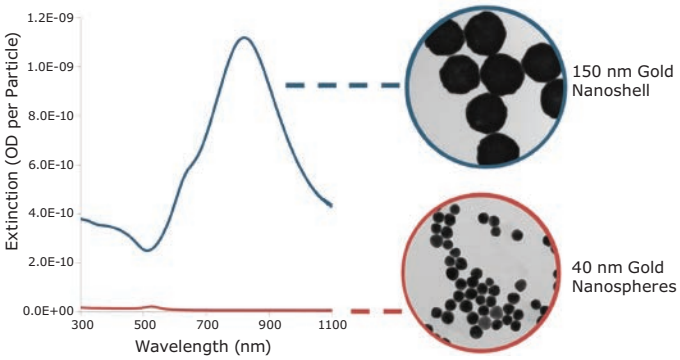

Figure 5. Per particle optical extinction (optical density per particle) as a function of wavelength for 40 nm gold nanospheres and 150 gold nanoshells.

(scattering + absorption) per particle of 40 nm gold nanospheres and 150 nm nanoshells. Because of their stronger extinction per particle, each nanoshell binding event exhibits a much higher contrast against the nitrocellulose substrate, resulting in increased assay sensitivity.

Figure 6 shows test and control lines using gold nanoshell reporters, with a corresponding scanning electron microscope image. Individual nanoshells bound to antibodies and then immobilized on the nitrocellulose membrane can be seen as light-colored spheres on the darker nitrocellulose fibers. Even at the relatively low coverage density on the membrane, the control line appears very dark, demonstrating that each nanoshell binding event generates a high contrast signal against the white nitrocellulose background.

Ultimately, the sensitivity of the assay is determined by the number of reporters that must bind to see a visible test line. To measure the number of particles required to obtain a visual signal, streptavidin-coated 40 nm gold nanospheres and

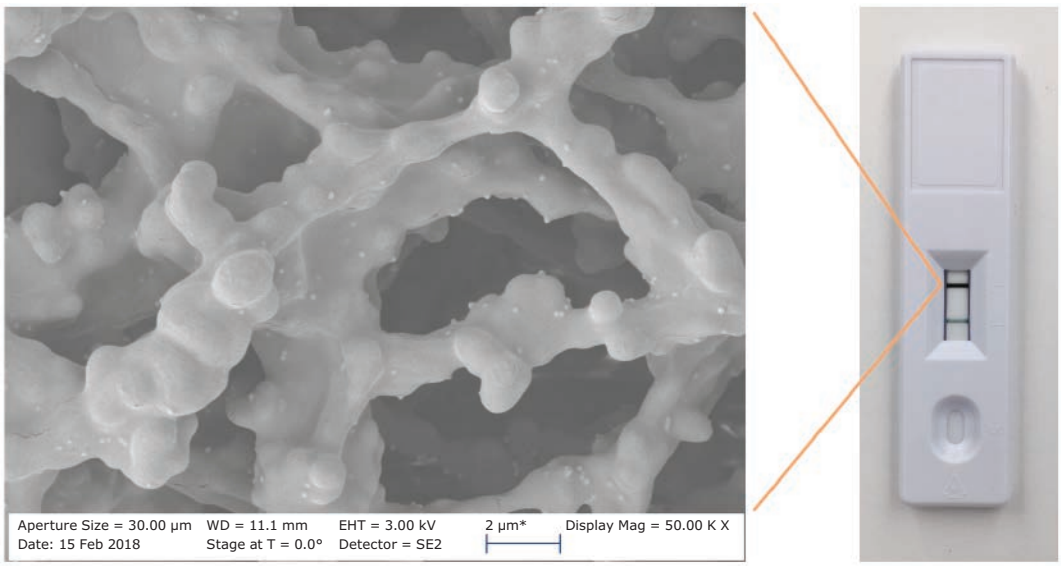

Figure 6. Gold nanoshells bound to a nitrocellulose membrane.

streptavidin-coated 150 nm gold nanoshells were captured on a biontinylated test line and the signal was analyzed with an optical reader (**Figure 7**). With 40 nm gold nanospheres there was a visible test line when 5 million particles were added to the assay. With gold nanoshells, only 500,000 particles were required to see a line, an order of magnitude decrease that yields increased assay sensitivity.

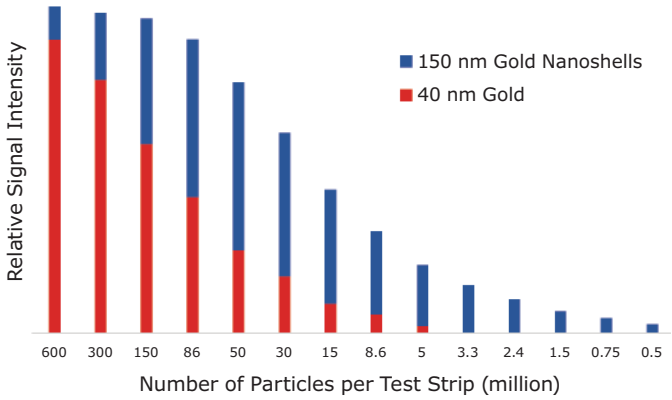

Figure 7. Lateral flow assay results where streptavidin-functionalized 150 nm gold nanoshells and 40 nm gold nanoparticles were placed on a nitrocellulose strip and captured on a biotinylated bovine serum albumin test line. The visual detection limit of gold nanospheres is 5,000,000, but for nanoshells it is 500,000 binding events.

To see how the absorbance per particle affects assay sensitivity, 40 nm diameter gold nanoparticles and 150 nm diameter gold nanoshells were used to detect Troponin I, a cardiac marker, in a lateral flow sandwich assay (**Figure 8**). The limit of detection with 40 nm gold nanoparticles was 0.5 ng/mL, while Troponin I detection with 150 nm gold nanoshells was an order of magnitude better at 0.05 ng/mL.

Covalent Linkage Chemistry for High Stability Reporters

Another important factor when developing high-sensitivity lateral flow assays is the method of binding antibodies or other proteins to the nanoparticle surface. Robust and effective binding is critical for maximizing both sensitivity and selectivity of the assay. The process of binding antibodies to the surface of a reporter particle is conjugation, and the resulting antibody-coated particle is called a conjugate.[4,5] Passive adsorption (physisorption) is the traditional method for attaching proteins to lateral flow nanoparticle probes, and is still widely used. By taking advantage of the forces between molecules and surfaces at a specific pH (e.g. van der Waals and ionic forces), antibodies can be made to spontaneously bind to a bare gold nanoparticle surface to form a conjugate. The antibody is typically added in excess, to ensure the entire surface of the nanoparticle is covered. Any antibody remaining free in solution after the conjugation is complete is removed via centrifugation or filtration.

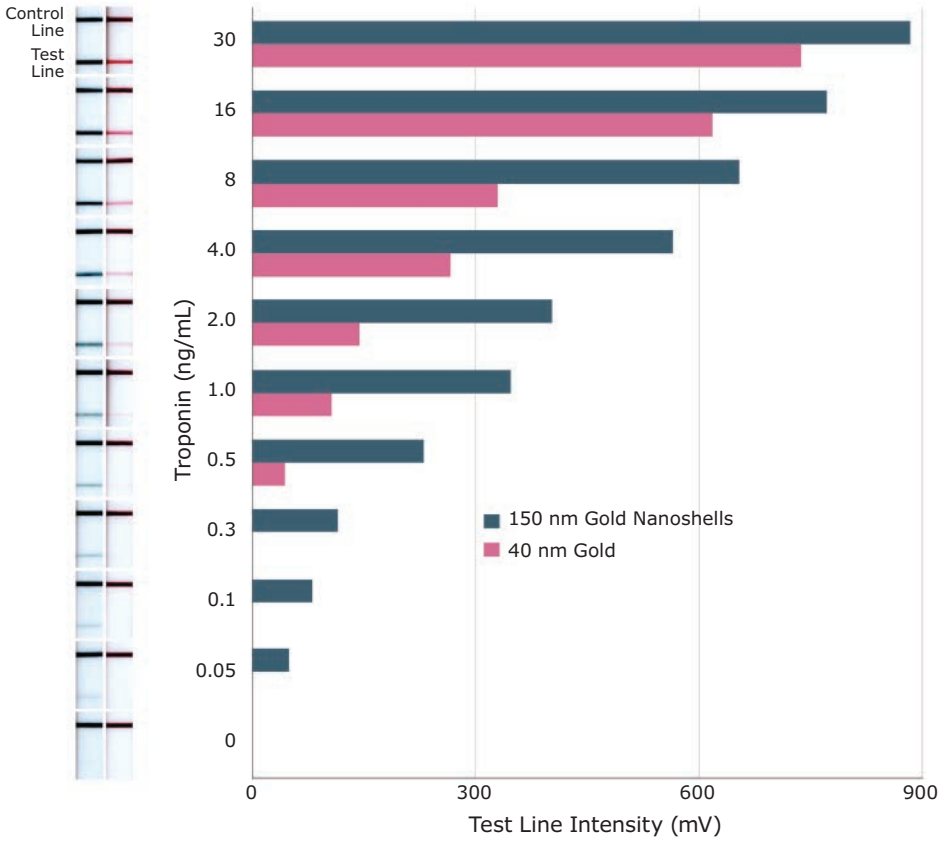

Figure 8. Sensitivity of lateral flow assay for Troponin I using 150 nm gold nanoshells and 40 nm gold nanospheres as reporter particles.

Conjugates can also be formed by covalently binding the antibody to the nanoparticle surface. Covalent binding is typically more reproducible than physisorption and for some antibodies, covalent chemistry is necessary to prepare stable conjugates. Covalent binding chemistry also allows for more control over the amount of antibody on the surface of the nanoparticles and the antibody orientation.

Other advantages of covalent binding include:

- Less antibody is needed to maximize sensitivity, reducing overall cost
- Covalent conjugates exhibit greater stability, allowing their use in difficult sample matrices and high salt/detergent buffering environments
- Conjugates are easily prepared without requiring extensive salt or pH optimizations, saving time when performing antibody screening experiments
- The antibody-to-particle ratio can be precisely controlled, which is important for adjusting the dynamic range in competitive assays and optimizing sensitivity with antibodies with varying binding kinetics

One common method of fabricating covalent conjugates utilizes carboxyl (carboxylic acid) functionalized gold surfaces. A carboxylic acid on the nanoparticle can be linked to a primary amine in the lysine residues of the antibody or protein using 1-Ethyl-3-(3-dimethylaminopropyl)carbodiimide (EDC) and N-hydroxysulfosuccinimide (sulfo-NHS) reagents to form amide bonds. A typical IgG antibody will have 80–100 lysine residues, of which 30–40 will be accessible for EDC/NHS binding.

Interpreting Results from Lateral Flow Tests

The results from a lateral flow test can be qualitative (if an analyte is or isn't present within the limits of detection), semi-quantitative (analyte present at low, medium, or high levels) or quantitative (precise amount of analyte present determined). The ubiquitous pregnancy test is an example of a qualitative "yes"/"no" assay, where a positive test line signal correlates to elevated levels of the hCG hormone in urine, indicating that the user is pregnant. For quantitative diagnostics, the test line intensities are compared to a calibration standard and converted to an analyte concentration value. Quantitative assays are used to measure the concentration of a specific analyte or biomarker, instead of simply indicating the presence or absence. For example, someone who experiences high stress may want to accurately measure the concentration of their cortisol levels over time, to determine if stress mitigation interventions are working. To accurately measure the test line intensity, the result must be analyzed by a strip reader. The recent commercialization of readers with a small form factor that are also inexpensive and mobile-centric is transforming the lateral flow assay industry. Simple methods that can quantify the output of lateral flow assays without requiring a stand-alone bench top reader opens a tremendous opportunity for home use and point-of-care diagnostics. **Figure 9** shows a variety of currently available disposable and benchtop reader formats. For benchtop units, a lateral flow cartridge is inserted into the instrument, the test and control line intensities are imaged with a camera, and the results are sent to a computer or mobile phone for display and interpretation. The calibration curve for any given assay can be encoded into the software, such that the test line signal intensity can be automatically converted to analyte concentration and presented to the user. Disposable readers have all of the necessary hardware to perform the analysis on the device itself, further simplifying the user experience.

Figure 9. Various Lumos Diagnostic reader formats for lateral flow diagnostics.

Conclusions

Ultra-bright reporter particles based on the unique optical properties of gold nanoshells significantly increase the sensitivity of lateral flow immunoassays. When combined with recent developments in portable reader technology, a new class of point-of-care diagnostics are coming to market that have the sensitivity, specificity, and reproducibility of laboratory-based tests but in a much less expensive and more convenient test format. In addition to lateral flow assays, gold nanoshells can be used in a wide variety of diagnostic and detection applications including surface enhanced Raman spectroscopy, flow cytometry, and molecular imaging. With simple covalent coupling chemistry and easy to follow protocols, gold nanoparticle conjugates are an important tool for many biotechnology applications.

References:

(1) Wong, R. C.; Tse, H. Y. *Lateral Flow Immunoassay*; Humana Press: New York, **2009**.
(2) Wilson, R. *Chem. Soc. Rev.* **2008**, *9*, 2028-2045.
(3) Oldenburg, S. J.; Averitt, R. D.; Westcott, S. L.; Halas, N. J. *Chem. Phys. Lett.* **1998**, *2*, 243-247.
(4) Hermanson, G.T. *Bioconjugate Techniques*; Academic Press, **2013**.
(5) *Nanomaterial Bioconjugation Techniques*, MilliporeSigma, **2017**.

Gold Nanoparticles and Nanostructures

Non-Surface Functionalized Nanoparticles

Gold Nanoparticles

Description	Particle Size (nm)	Adsorption (nm)	Concentration	Cat. No.
reactant free stabilized suspension in 0.1 mM PBS	5	510-525	~ 5.5E+13 particles/mL	**752568-25ML** **752568-100ML**
	20	518-522	~ 6.54E+11 particles/mL	**753610-25ML** **753610-100ML**
	50	535-536	~ 3.5E+10 particles/mL	**753645-25ML** **753645-100ML**
	100	564-574	~ 3.8E+9 particles/mL	**753688-25ML** **753688-100ML**
	40	529-533	~ 7.2E+10 particles/mL	**753637-25ML** **753637-100ML**
	15	510-520	~ 1.64E+12 particles/mL	**777099-25ML** **777099-100ML**
dispersion in H_2O silica coated	10	514-524	~ 7.1E+12 particles/mL	**747564-5ML**
	20	518-528	~ 8.5E+11 particles/mL	**747572-5ML**
	5	-	~ 6.6E+13 particles/mL	**747556-5ML**
stabilized suspension in citrate buffer	5	510-525	~ 5.5E+13 particles/mL	**741949-25ML** **741949-100ML**
	20	518-522	~ 6.54E+11 particles/mL	**741965-25ML** **741965-100ML**
	40	529-533	~ 7.2E+10 particles/mL	**741981-25ML** **741981-100ML**
	50	533-536	~ 3.5E+10 particles/mL	**742007-25ML** **742007-100ML**
	80	551-557	~ 7.8E+9 particles/mL	**742023-25ML** **742023-100ML**
	100	564-574	~ 3.8E+9 particles/mL	**742031-25ML** **742031-100ML**

Gold Nanospheres

Description	Particle Size (nm)	Cat. No.
Bare Bioready for Passive Adsorption in Aqueous Sodium Citrate	40	**NCXAUCR40-5M** **NCXAUCR40-30ML** **NCXAUCR40-100ML**
Bare Bioready Carbonate for Passive Adsorption in Water	40	**NCXAUKR40-5ML** **NCXAUKR40-30ML** **NCXAUKR40-100ML**
Bare Bioready Carbonate for Passive Adsorption in Aqueous Potassium Carbonate	80	**NCXAUKR80-25ML** **NCXAUKR80-100ML** **NCXAUKR80-500ML** **NCXAUKR80-1000ML**

Non-Surface Functionalized Nanostructures

Gold Nano-urchins

Particle Size (nm)	Adsorption (nm)	Cat. No.
60	585	**795399-25ML**
50	585	**795380-25ML**
100	680	**797758-25ML**
70	600	**797731-25ML**
80	620	**797723-25ML**
90	630	**797707-25ML**

Gold Nanorods

Particle Size (nm)	Absorption	Concentration (µg/mL)	Cat. No.
10	780 nm	> 30 in H_2O	**747971-5ML**
	808 nm	> 30 in H_2O	**747998-5ML**
	850 nm	> 30 in H_2O	**748005-5ML**
	980 nm	> 30 in H_2O	**776661-25ML**
25	550 nm	> 45 in H_2O	**771643-25ML**
	650 nm	> 45 in H_2O	**771686-25ML**
10	780 nm	35 in H_2O	**900362-25ML**

Particle Size (nm)	Absorption	Concentration (µg/mL)	Cat. No.
25	650 nm	50 in H_2O	**900367-25ML**
10	808 nm	35 in H_2O	**900363-25ML**
25	550 nm	50 in H_2O	**900366-25ML**
10	980 nm	35 in H_2O	**900364-25ML**
	1064 nm	35 in H_2O	**900365-25ML**

Surface Functionalized Nanoparticles and Nanostructures

Gold Nanoparticles

Description	Dimension (nm)	Absorption nm	Cat. No.
PEG 2000 coated methyl terminated	15	520	**765694-1ML**
	20	520	**765716-1ML**
PEG 3000 coated amine functionalized	5	515	**765260-1ML**
	15	520	**765317-1ML**
	30	525	**765368-1ML**
	50	535	**765406-1ML**
PEG 3000 coated carboxylic acid functionalized	5	515	**765430-1ML**
	15	520	**765473-1ML**
	30	525	**765538-1ML**
	50	535	**765570-1ML**
PEG 5000 coated amine functionalized	5	515	**765279-1ML**
	15	520	**765325-1ML**
	30	525	**765376-1ML**
	50	535	**765414-1ML**
PEG 5000 coated biotin terminated	100	572	**808962-0.5ML**
	80	553	**808946-0.5ML**
	40	530	**808865-0.5ML**
	20	524	**808849-0.5ML**
PEG 5000 coated carboxylic acid functionalized	10	530	**765465-1ML**
	20	520	**765511-1ML**
	50	535	**765589-1ML**
PEG 5000 coated methyl terminated	5	515	**765600-1ML**
	30	525	**765732-1ML**
	50	535	**765686-1ML**

Gold Nanorods

Description	Dimension (nm)	Absorption nm	Cat. No.
amine terminated	10	808	**716871-1ML**
carboxyl terminated	10	808	**716898-1ML**

Gold Nanoshells

Description	Absorption	Concentration (mg/mL)	Cat. No.
NanoXact PVP 40 kDa (Polymer)	660 nm	1 in water	**NCXGSPH660-500UL** **NCXGSPH660-1ML** **NCXGSPH660-5ML**
	800 nm	1 in water	**NCXGSPH800-500UL** **NCXGSPH800-1ML** **NCXGSPH800-5ML**
	980 nm	1 in water	**NCXGSPH980-500UL** **NCXGSPH980-1ML** **NCXGSPH980-5ML**
Carboxyl (Lipoic Acid) NanoXact	660 nm	1 in water	**NCXGSLH660-500UL** **NCXGSLH660-1ML** **NCXGSLH660-5ML**
	800 nm	1 in water	**NCXGSLH800-500UL** **NCXGSLH800-1ML** **NCXGSLH800-5ML**
	980 nm	1 in water	**NCXGSLH980-500UL** **NCXGSLH980-1ML** **NCXGSLH980-5ML**
NanoXact mPEG 5 kDa (Polymer)	660 nm	1 in water	**NCXGSGH660-500UL** **NCXGSGH660-1ML** **NCXGSGH660-5ML**
	800 nm	1 in water	**NCXGSGH800-500UL** **NCXGSGH800-1ML** **NCXGSGH800-5ML**
	980 nm	1 in water	**NCXGSGH980-500UL** **NCXGSGH980-1ML** **NCXGSGH980-5ML**

Description	Absorption (nm)	Concentration (mg/mL)	Cat. No.
NanoXact PVP 40 kDa (Polymer)	660	0.05 in water	**NCXGSPN660-25ML** **NCXGSPN660-100ML** **NCXGSPN660-500ML**
	800	0.05 in water	**NCXGSPN800-25ML** **NCXGSPN800-100ML** **NCXGSPN800-500ML**
	980	0.05 in water	**NCXGSPN980-25ML** **NCXGSPN980-100ML** **NCXGSPN980-500ML**
Carboxyl (Lipoic Acid) NanoXact	660	0.05 in water	**NCXGSLN660-25ML** **NCXGSLN660-100ML** **NCXGSLN660-500ML**
	800	0.05 in water	**NCXGSLN800-25ML** **NCXGSLN800-100ML** **NCXGSLN800-500ML**
	980	0.05 in water	**NCXGSLN980-25ML** **NCXGSLN980-100ML** **NCXGSLN980-500ML**
NanoXact mPEG 5 kDa (Polymer)	660	0.05 in water	**NCXGSGN660-25ML** **NCXGSGN660-100ML** **NCXGSGN660-500ML**
	800	0.05 in water	**NCXGSGN800-25ML** **NCXGSGN800-100ML** **NCXGSGN800-500ML**
	980	0.05 in water	**NCXGSGN980-25ML** **NCXGSGN980-100ML** **NCXGSGN980-500ML**

Gold Nanospheres

Description	Dimension (nm)	Cat. No.
Bioready Carboxyl for Covalent Conjugation in Water	40	**NCXAUXR40-5ML** **NCXAUXR40-30ML** **NCXAUXR40-100ML**
	80	**NCXAUXR80-5ML** **NCXAUXR80-30ML** **NCXAUXR80-100ML**
Bioready Streptavidin in Aqueous Conjugate Buffer with Streptavidin	40	**NCXAUIR40-200UL** **NCXAUIR40-1ML** **NCXAUIR40-5ML** **NCXAUIR40-10ML**
NanoXact Silica (Silanol) Silica-Shelled	20	**NCXAUSH20-1ML** **NCXAUSH20-5ML** **NCXAUSH20-10ML**
	50	**NCXAUSH50-1ML** **NCXAUSH50-5ML** **NCXAUSH50-10ML**
	100	**NCXAUSH100-1ML** **NCXAUSH100-5ML** **NCXAUSH100-10ML**
Aminated / Cationic Silica NanoXact Silica-Shelled	20	**NCXAUAH20-1ML** **NCXAUAH20-5ML** **NCXAUAH20-10ML**
	50	**NCXAUAH50-1ML** **NCXAUAH50-5ML** **NCXAUAH50-10ML**
	100	**NCXAUAH100-1ML** **NCXAUAH100-5ML** **NCXAUAH100-10ML**
Econix PVP 40 kDa (Polymer)	15	**NCXGEPE15-10ML** **NCXGEPE15-25ML** **NCXGEPE15-100ML**
	50	**NCXGEPE50-10ML** **NCXGEPE50-25ML** **NCXGEPE50-100ML**
	75	**NCXGEPE75-10ML** **NCXGEPE75-25ML** **NCXGEPE75-100ML**
Dried Econix PVP 40 kDa (Polymer)	15	**NCXGEPD15-50MG** **NCXGEPD15-125MG** **NCXGEPD15-500MG**
	50	**NCXGEPD50-50MG** **NCXGEPD50-125MG** **NCXGEPD50-500MG**
	75	**NCXGEPD75-50MG** **NCXGEPD75-125MG** **NCXGEPD75-500MG**

Description	Dimension (nm)	Cat. No.
PEG Carboxyl 0.8 kDa Ultra Uniform	10	**NCXAUXU10-1ML** **NCXAUXU10-5ML** **NCXAUXU10-10ML** **NCXAUXU10-30ML**
	50	**NCXAUXU50-1ML** **NCXAUXU50-5ML** **NCXAUXU50-10ML** **NCXAUXU50-30ML**
	100	**NCXAUXU100-1ML** **NCXAUXU100-5ML** **NCXAUXU100-10ML** **NCXAUXU100-30ML**

Surface Functionalized Nanoparticles and Nanostructure Kits

Gold Nanoparticles

Functional Group	Particle Size (nm)	Absorption (nm)	Cat. No.
maleimide	5	515-520	**900458-1EA**
	10	515-520	**900459-1EA**
	40	530	**900463-1EA**
	50	535	**900464-1EA**
	90	564	**900468-1EA**
	100	572	**900469-1EA**
NHS ester	5	515-520	**900470-1EA**
	10	515-520	**900473-1EA**
	40	530	**900477-1EA**
	50	535	**900478-1EA**
	90	564	**900482-1EA**
	100	572	**900483-1EA**

Nanoshells

Name	Particle Size (nm)	Cat. No.
Gold Nanoshells	150	**NCXGSNR1501L-1KT**
	150	**NCXGSNR1503S-1KT**
	150	**NCXGSNR15010S-1KT**

Nanospheres

Name	Particle Size (nm)	Cat. No.
Gold Nanospheres	40	**NCXAUNR403S-1KT**
	40	**NCXAUNR4010S-1KT**
	40	**NCXAUNR401L-1KT**

Nano-urchins

Functional Group	Particle Size (nm)	Absorption (nm)	Cat. No.
maleimide	50	585	**900484-1EA**
	70	600	**900486-1EA**
	90	630	**900488-1EA**
	100	680	**900489-1EA**
NHS ester	50	585	**900490-1EA**
	70	600	**900492-1EA**
	90	630	**900494-1EA**
	100	680	**900495-1EA**

MilliporeSigma
400 Summit Drive
Burlington, MA 01803

Materials Research Society Mid-Career Researcher Award Recipient

Hongyou Fan
Sandia National Laboratories &
The University of New Mexico

"For outstanding contributions in nanoparticle self-assembly of functional nanomaterials and for leadership within the materials community"

Hongyou Fan is a Distinguished Member of the Technical Staff at Sandia National Laboratories and is a National Laboratory Professor in the Department of Chemical and Biological Engineering at The University of New Mexico. He received a BS degree in chemistry from Jilin University in 1990, an MS degree in polymer science from the Chinese Academy of Sciences in 1995, and a PhD degree in chemical engineering from The University of New Mexico in 2000. He was a Postdoctoral Fellow at Sandia National Laboratories before working there full-time. His research focuses on functional nanomaterials synthesis, assembly and integration for nanoelectronic and nanophotonic applications. Fan is a Fellow of the American Physical Society and the Materials Research Society (MRS). Prior to the MRS Mid-Career Researcher Award, he received the MRS Fred Kavli Distinguished Lectureship Award in Nanoscience, four R&D 100 Awards for the development of technically significant products, two Federal Laboratory Consortium for Technology Transfer–Outstanding Technology Development Awards, The University of New Mexico Outstanding Faculty Mentor Award, and the Asian American Engineer of the Year Award.

Mid-Career Researcher Award is endowed by the life science business of Merck KGaA, Darmstadt, Germany, which operates as MilliporeSigma in the U.S. and Canada.